



UNIVERSITY OF LEEDS

This is a repository copy of *Elucidating the Role of Ligand Engineering on Local and Macroscopic Charge-Carrier Transport in NaBiS<sub>2</sub> Nanocrystal Thin Films*.

White Rose Research Online URL for this paper:

<https://eprints.whiterose.ac.uk/214976/>

Version: Published Version

---

**Article:**

Huang, Y., Schleuning, M., Hempel, H. et al. (16 more authors) (2024) Elucidating the Role of Ligand Engineering on Local and Macroscopic Charge-Carrier Transport in NaBiS<sub>2</sub> Nanocrystal Thin Films. *Advanced Functional Materials*. ISSN 1616-301X

<https://doi.org/10.1002/adfm.202310283>

---

**Reuse**

This article is distributed under the terms of the Creative Commons Attribution (CC BY) licence. This licence allows you to distribute, remix, tweak, and build upon the work, even commercially, as long as you credit the authors for the original work. More information and the full terms of the licence here:

<https://creativecommons.org/licenses/>

**Takedown**

If you consider content in White Rose Research Online to be in breach of UK law, please notify us by emailing [eprints@whiterose.ac.uk](mailto:eprints@whiterose.ac.uk) including the URL of the record and the reason for the withdrawal request.



[eprints@whiterose.ac.uk](mailto:eprints@whiterose.ac.uk)  
<https://eprints.whiterose.ac.uk/>

# Elucidating the Role of Ligand Engineering on Local and Macroscopic Charge-Carrier Transport in NaBiS<sub>2</sub> Nanocrystal Thin Films

Yi-Teng Huang, Markus Schleuning, Hannes Hempel, Youcheng Zhang, Marin Rusu, Thomas Unold, Artem Musiienko, Orestis Karalis, Nora Jung, Szymon J. Zelewski, Andrew J. Britton, Natalie Ngoh, Weixin Song, Louise C. Hirst, Henning Sirringhaus, Samuel D. Stranks, Akshay Rao, Igal Levine,\* and Robert L. Z. Hoyer\*


Ternary chalcogenides have emerged as potential candidates for ultrathin photovoltaics, and NaBiS<sub>2</sub> nanocrystals (NCs) have gained appeal because of their months-long phase-stability in air, high absorption coefficients  $>10^5 \text{ cm}^{-1}$ , and a pseudo-direct bandgap of 1.4 eV. However, previous investigations into NaBiS<sub>2</sub> NCs used long-chain organic ligands separating individual NCs during synthesis, which severely limits macroscopic charge-carrier transport. In this work, these long-chain ligands are exchanged for short iodide-based ligands, allowing to understand the macroscopic charge-carrier transport properties of NaBiS<sub>2</sub> and evaluate its photovoltaic potential in more depth. It is found that ligand exchange results in simultaneous improvements in intra-NC (microscopic) and inter-NC (macroscopic) mobilities, while charge-carrier localization still takes place, which places a fundamental limit on the transport lengths achievable. Despite this limitation, the high absorption coefficients enable ultrathin (55 nm thick) solar absorbers to be used in photovoltaic devices, which have peak external quantum efficiencies  $> 50\%$ . In addition, temperature-dependent transient current measurements uncover a small activation energy barrier of 88 meV for ion migration, which accounts for the strongly hysteretic behavior of NaBiS<sub>2</sub> photovoltaic devices. This work not only reveals how the charge-carrier transport properties of NaBiS<sub>2</sub> NCs over several length and time scales are influenced by ligand engineering, but also unveils the facile ionic transport in this material, which limits the potential of NaBiS<sub>2</sub> in photovoltaics. On the other hand, the discovery shows that there are opportunities to use this material in memristors, electrolytes, and other applications requiring ionic conduction.

## 1. Introduction

With outstanding optoelectronic properties and solution processibility, lead-halide perovskites (LHPs) have made great progress in the field of photovoltaics (PVs) over the past decade.<sup>[1]</sup> However, concerns over lead toxicity and the instability of LHPs have motivated investigations into lead-free alternatives that are their chemical analogs (e.g., MASnI<sub>3</sub>, where MA = CH<sub>3</sub>NH<sub>3</sub><sup>+</sup>), structural analogs (e.g., halide elpasolites), or electronic analogs (e.g., BiOI). Collectively, all these compounds are termed “perovskite-inspired materials”, or PIMs.<sup>[2–4]</sup> Early studies on PIMs mainly focused on metal-halide compounds, such as FASnI<sub>3</sub>, Cs<sub>3</sub>Bi<sub>2</sub>I<sub>9</sub>, and BiI<sub>3</sub>, while chalcogenides gradually drew more attention in recent years because of their high stability, as well as promising improvements in PV efficiency.<sup>[4,5]</sup>

In particular, I-V-VI<sub>2</sub> ternary chalcogenides, or ABZ<sub>2</sub> materials, are one of the most promising bismuth-based absorbers reported so far. One of the highest power conversion efficiencies (PCEs) among all bismuth-based PV devices (9.17%; 8.85% certified) was achieved in a solar cell

Y.-T. Huang, R. L. Z. Hoyer  
Inorganic Chemistry Laboratory  
Department of Chemistry  
University of Oxford  
South Parks Road, Oxford OX1 3QR, UK  
E-mail: robert.hoyer@chem.ox.ac.uk

 The ORCID identification number(s) for the author(s) of this article can be found under <https://doi.org/10.1002/adfm.202310283>

© 2024 The Authors. Advanced Functional Materials published by Wiley-VCH GmbH. This is an open access article under the terms of the [Creative Commons Attribution](#) License, which permits use, distribution and reproduction in any medium, provided the original work is properly cited.

DOI: 10.1002/adfm.202310283

Y.-T. Huang, Y. Zhang, S. J. Zelewski, L. C. Hirst, H. Sirringhaus,  
S. D. Stranks, A. Rao  
Cavendish Laboratory  
University of Cambridge  
JJ Thomson Ave, Cambridge CB3 0HE, UK  
M. Schleuning  
Institut für Chemie  
Technische Universität Berlin  
Straße des 17. Juni 124, 10623 Berlin, Germany

based on a  $\text{AgBiS}_2$  absorber that was only 30 nm thick, showing ABZ<sub>2</sub> materials to have great potential for ultrathin PV applications.<sup>[5]</sup> Very recently,  $\text{NaBiS}_2$  nanocrystals (NCs) were identified as another promising ABZ<sub>2</sub> material, composed of earth-abundant, cost-effective, and nontoxic elements.<sup>[6,7]</sup> Owing to the concentrated density of states (DOS) near the band edges,  $\text{NaBiS}_2$  NCs exhibit high absorption coefficients exceeding  $10^5 \text{ cm}^{-1}$  at and beyond their pseudo-direct bandgap of 1.4 eV (where the energy difference between the indirect bandgap and first direct transition is only 0.01 eV), leading to a calculated spectroscopic limited maximum efficiency (SLME) of 26% under 1-sun illumination from a 30 nm-thick film. Moreover,  $\text{NaBiS}_2$  NCs could retain their phase-purity and appearance under ambient conditions for at least 11 months, indicating the high air stability of this material. These notable features could potentially enable the realization of ultrathin, flexible, and lightweight electronic devices. However,  $\text{NaBiS}_2$  also has a similar cation-disordered phase (space group:  $Fm\bar{3}m$ ) as  $\text{AgBiS}_2$ , in which the two metal cations ( $\text{Na}^+$  and  $\text{Bi}^{3+}$ ) can randomly occupy the same crystallographic lattice site due to their similar ionic radii. From our previous work, it has been found that the wavefunctions of

free electrons and holes created after photo-excitation could be localized to varying degrees at  $\text{Bi}^{3+}$ - and  $\text{Na}^+$ -rich clusters, respectively. In particular,  $\text{Na}^+$  clusters result in S 3p states forming just above the valence band maximum (VBM), which can strongly localize holes to form small polarons. As a result, the sum mobility of  $\text{NaBiS}_2$  NC films was found to reduce substantially from 0.29 to 0.03  $\text{cm}^2 \text{ V}^{-1} \text{ s}^{-1}$  within 1 ps after photo-excitation.<sup>[7]</sup>

The charge-carrier transport properties of  $\text{NaBiS}_2$  studied thus far have only been limited to the intra-NC level. The “macroscopic transport” across several NCs could be further reduced by long-chain oleylamine (OLA) and oleic acid (OA) ligands coordinated to the surface of the NCs. Although these organic ligands are essential for the colloidal solubility of NCs in non-polar solvents (e.g., toluene) during synthesis, their insulating nature inhibits the transport of charge-carriers between NCs. Therefore, ligand exchange treatment, which refers to the replacement of long-chain organic ligands with other short-chain ligands, is a crucial step in fabricating NC-based devices. Additionally, ligand exchange could alter the surface stoichiometry or dipole moments formed between the NC surface and ligands,<sup>[8]</sup> leading to changes in the electronic band structure and hence optoelectronic properties (e.g., shifts in energy levels<sup>[8–10]</sup> or doping levels)<sup>[11,12]</sup> of materials. As a result, devices based on NCs treated by different ligands could show distinctive performance.<sup>[8,13]</sup>

Medina-Gonzalez et al. have indicated that after the ligand exchange treatment using several halides, the original insulating  $\text{NaBiS}_2$  NC films coordinated by long-chain organic ligands could show a detectable conductivity on the order of  $10^{-4}$ – $10^{-6} \text{ S cm}^{-1}$ .<sup>[14]</sup> However, how these halides affect the optoelectronic properties of  $\text{NaBiS}_2$  NCs and whether these halide-treated films could be applied in practical devices remain open questions. In this work, we aim to comprehensively investigate the impact of ligand exchange on the absorption spectrum, crystal structure, and more importantly, charge-carrier transport of  $\text{NaBiS}_2$  NCs. Herein, LiI, NaI, KI, and tetramethylammonium iodide (TMAI) were investigated for ligand exchange, and their effectiveness in substituting the original long-chain ligands were first confirmed from Fourier-transform Infrared (FTIR) spectroscopy. We hypothesize that both the electronic band structure of single NC and the spacing between NCs are modified simultaneously during ligand exchange treatment, which could lead to significant changes to the charge-carrier dynamics at different length and time scales. To test this hypothesis, we first measured the absorption spectra, surface composition, crystal structure, and surface photovoltage (SPV), along with the valence band density of states (VB DOS) to gain insights into the electronic band structure of  $\text{NaBiS}_2$  NCs after ligand exchange treatment. Next, optical-pump-terahertz-probe (OPTP) spectroscopy and time-resolved microwave conductivity (TRMC) measurements were used to probe the charge-carrier dynamics of both pristine and iodide-treated samples over different time scales. Finally,  $\text{NaBiS}_2$  solar cells based on iodide-treated NC films were fabricated and tested. Surprisingly, strong hysteresis was found in  $\text{NaBiS}_2$  solar cells, and temperature-dependent transient current measurements were performed to understand ionic conduction in this material.

M. Schleuning  
Chemical Energy Division  
Helmholtz-Zentrum Berlin für Materialien und Energie GmbH,  
Hahn-Meitner-Platz 1  
14109 Berlin, Germany  
H. Hempel, M. Rusu, T. Unold, A. Musiienko, O. Karalis, N. Jung,  
I. Levine  
Solar Energy Division  
Helmholtz-Zentrum Berlin für Materialien und Energie GmbH  
Hahn-Meitner-Platz 1, 14109 Berlin, Germany  
E-mail: [igal.levine@mail.huji.ac.il](mailto:igal.levine@mail.huji.ac.il)  
S. J. Zelewski  
Department of Experimental Physics  
Faculty of Fundamental Problems of Technology  
Wrocław University of Science and Technology  
Wybrzeże Wyspiańskiego 27, Wrocław 50–370, Poland  
A. J. Britton  
School of Chemical and Process Engineering  
University of Leeds  
Leeds LS2 9JT, UK  
N. Ngoh  
Department of Materials  
Imperial College London  
Exhibition Road, London SW7 2AZ, UK  
W. Song  
Department of Materials  
University of Oxford  
Oxford OX2 6NN, UK  
L. C. Hirst  
Department of Materials Science and Metallurgy  
University of Cambridge  
Cambridge CB3 0FS, UK  
S. D. Stranks  
Department of Chemical Engineering & Biotechnology  
University of Cambridge  
Philippa Fawcett Drive, Cambridge CB3 0AS, UK  
I. Levine  
Institute of Chemistry  
The Hebrew University  
Jerusalem 91904, Israel

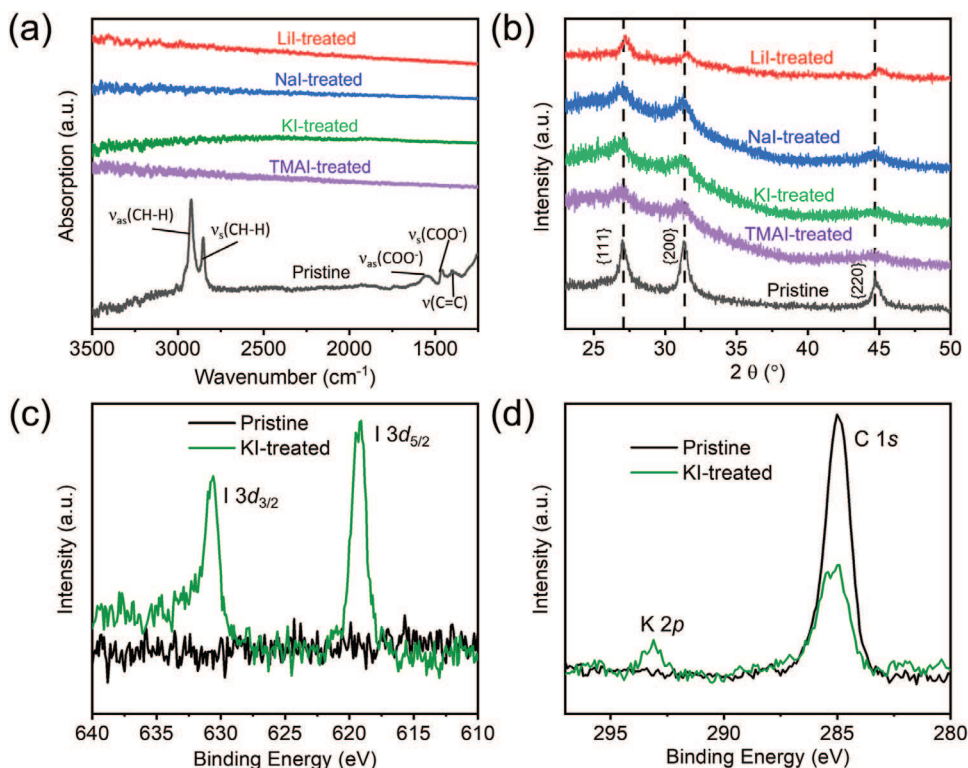


**Figure 1.** The effect of ligand exchange on the structural properties and surface composition of NaBiS<sub>2</sub> nanocrystal (NC) films. a) Fourier-transform infrared (FTIR) spectra and b) X-ray diffraction (XRD) patterns of the pristine and iodide-treated NaBiS<sub>2</sub> NC films. The black dashed lines refer to the peak position of each XRD peak in the pristine film. The near-ambient pressure X-ray photoelectron spectra (XPS) of c) I 3d, d) C 1s, as well as K 2p for the pristine and KI-treated NaBiS<sub>2</sub> NC film. The pristine films were prepared by drop-casting, while the iodide-treated films were prepared by the layer-by-layer (LBL) deposition process up to a thickness of ~300 and 55 nm for XRD and XPS measurements, respectively.

## 2. Results and Discussion

### 2.1. Effectiveness of Ligand Exchange Treatment

Herein, we first tested the effectiveness of ligand exchange by using various halide salts dissolved in methanol. To ensure the complete removal of organic ligands, we waited for up to 2 min after dropping the 0.1 M halide salt solutions onto the spin-coated NaBiS<sub>2</sub> NC films. Among our tested halide salts (including NaCl, NaBr, KCl, KBr, LiI, NaI, KI, and tetramethylammonium iodide, or TMAI), we found that LiI, NaI, KI, and TMAI were the most effective at replacing the original long-chain organic ligands with iodide anions and/or alkali/alkylammonium cations, whilst maintaining a compact film morphology (Figure S1, Supporting Information). As can be seen from Figure 1a, the absence of vibrational signals from carboxyl groups in the Fourier-transform infrared (FTIR) spectra of the iodide-treated films indicates a substantial replacement of the original oleate ligands after exchange. Transmission electron microscopy (TEM) images (Figure S2, Supporting Information) also show that the NCs tended to pack more closely after ligand exchange treatment compared to the pristine NCs, suggesting that the inter-NC distance has been reduced due to the use of shorter ligands.

Hereafter, we compared the pristine NC films with ligand-exchanged (iodide-treated) NC films. The pristine NC films were prepared by drop-casting the purified NC solution, while the iodide-treated films were prepared by the layer-by-layer (LBL) de-

position process (as detailed in the Experimental section). Note that such a process cannot be used for the pristine films because each layer of the NaBiS<sub>2</sub> NC film deposited would be washed away when spin-coating any NaBiS<sub>2</sub> NC solution on top. On the other hand, after changing these long-chain organic ligands for short inorganic ligands, NCs became no longer soluble in non-polar solvents, and were therefore not washed away when another layer of NCs dissolved in non-polar toluene was spin-coated on top.

### 2.2. Structural Characterization

The effect of ligand exchange on the crystal structure was examined by comparing the X-ray diffraction (XRD) patterns of the pristine film and iodide-treated films. Herein, larger NaBiS<sub>2</sub> NCs synthesized at 150 °C (mean size of 18 ± 4 nm)<sup>[7]</sup> were used in order to fully resolve the small peak differences between the pristine and iodide-treated NC films. To be clear, these larger NaBiS<sub>2</sub> NCs were only used for XRD measurements, whilst smaller NaBiS<sub>2</sub> NCs synthesized at 80 °C (mean size 4.0 ± 1.0 nm, see the TEM image in the Figure S2a, Supporting Information) were used in all of the following experiments because of their better colloidal stability. We showed in our previous work that the phase purity and air stability of NCs with both sizes are similar.<sup>[7]</sup>

As shown in Figure 1b, the pristine and all of the iodide-treated NaBiS<sub>2</sub> NC films exhibit a rocksalt cubic structure (space group: *Fm* $\bar{3}$ *m*). Note that the weaker peak intensity in the XRD patterns

of the iodide-treated films is due to their much smaller film thickness ( $\sim 300$  nm) compared to the drop-cast pristine film (a few  $\mu\text{m}$ ). Comparing the iodide-treated films with the pristine film, we could only observe a small peak shift ( $< 0.3^\circ$  in  $2\theta$ ) toward larger Bragg angles, indicating a minimal reduction of less than  $0.02$  Å in the lattice parameter. These small changes imply that ligand exchange treatment on  $\text{NaBiS}_2$  might not significantly improve its cation inhomogeneity, which is predicted to result in shorter cation-anion bond lengths.<sup>[7]</sup>

To investigate the impact of ligand exchange treatment on the surface composition of the NCs, near-ambient pressure X-ray photoelectron spectroscopy (XPS) measurements were performed on the pristine and KI-treated  $\text{NaBiS}_2$  film. We conducted the XPS measurements under near-ambient pressure (7 mbar) because it was previously found that Na could be easily lost in ultra-high vacuum (e.g., in conventional XPS or during energy dispersive X-ray spectrometry measurements).<sup>[7]</sup> Herein, only the KI-treated film was characterized for comparison with the pristine sample because the sensitivity for Li or Na signals was relatively low, and it is challenging to distinguish the N and C species in  $\text{TMA}^+$  cations from those already present on the pristine  $\text{NaBiS}_2$  film surface. From Figure 1c,d, we can see a decrease in the C 1s peak intensity, along with the appearance of I 3d and K 2p signals in the KI-treated film. These results again indicate that most organic ligands were replaced by iodides, and A-site cations could also be incorporated/doped into the film during ligand exchange, which could potentially alter the electronic band structure of  $\text{NaBiS}_2$ . Surprisingly, although bismuth (Bi 4f, Figure S3a, Supporting Information) and sulfur (S 2s, Figure S3b, Supporting Information) peaks could be seen in both the pristine and KI-treated films, we could not detect Na signals in either of them, which is different from the Na-rich NC surface found in our previous work.<sup>[7]</sup> This difference might be associated with the fact that we used toluene rather than hexane, which was used in our previous work,<sup>[7]</sup> to dissolve  $\text{NaBiS}_2$  NCs here in order to improve film morphology (Figure S1, Supporting Information). Although  $\text{NaBiS}_2$  NCs could be completely dissolved in both toluene and hexane, surface sodium-based species might be gradually removed in toluene due to its higher relative polarity (0.099, cf. hexane: 0.009). Despite this Na-poor surface, we note that the bulk phase of the KI-treated film remains  $\text{NaBiS}_2$  rather than  $\text{KBiS}_2$ , as verified from the XRD patterns in Figure S4 (Supporting Information). This result indicates that Na compounds should be still present in the bulk region of the KI-treated film, and  $\text{KBiS}_2$  is unlikely to be formed. The  $\text{NaBiS}_2$  films treated by other iodides were also verified to remain in the same phase, as displayed in Figure 1b.

In addition, both the pristine and KI-treated films showed a similar valence band to Fermi level offset of  $\sim 1$  eV (Figure S3c, Supporting Information). These results are in good agreement with the energy levels measured from photoelectron yield spectroscopy (PYS) and Kelvin Probe (KP) measurements ( $\sim 1.15$  eV, Figure S5, Supporting Information), which could determine the ionization potentials  $E_i$  and work functions  $\Phi$  of the materials, respectively. Note that compared to the KI-treated film, the pristine film showed a less obvious primary edge in its valence spectrum, which could be attributed to the stronger photoelectron scattering caused by a large number of organic ligands covering the surface.

### 2.3. Influence of Ligand Exchange on Optoelectronic Properties

Next, we compared the absorption coefficient spectra of the pristine and iodide-treated films. To acquire the absorption coefficient spectra, a combination of photothermal deflection spectroscopy (PDS) and ultraviolet-visible spectrophotometry (UV-Vis) measurements were used (see details in the Experimental Section). Since PDS can detect very minor temperature changes caused by non-radiative recombination processes when the materials are illuminated, it can precisely determine the relative absorbance profile even in the weakly-absorbing sub-gap region. On the other hand, UV-Vis, performed using an integrating sphere, can be used to determine the absolute absorption coefficients. The complete absorption coefficient spectra extending to the sub-gap region can therefore be obtained by scaling the relative absorbance acquired from PDS to match the absolute absorption coefficient values acquired from UV-Vis.

From Figure 2a, we can see that all iodide-treated films showed lower absorption coefficients in the 1.25–2.7 eV photon energy ( $h\nu$ ) range compared to the pristine film, which is opposite to the trend in the  $\text{AgBiS}_2$  films with more homogeneous cation distributions.<sup>[5]</sup> This result hence suggests that the inhomogeneity of cation disorder might not be mitigated following ligand exchange, but the electronic band structure of the iodide-treated films could be changed, leading to lower absorption coefficients as a result from reduced transition dipole moments. Surprisingly, although TMAI has been commonly used in ligand exchange treatment for  $\text{AgBiS}_2$  NCs,<sup>[15,16]</sup> the TMAI-treated  $\text{NaBiS}_2$  film showed increased sub-gap absorption below 1.25 eV  $h\nu$ , implying that extra in-gap defect states could be introduced during treatment, possibly because of the polar nature of the methanol solvent used for ligand exchange. On the other hand, we do not observe similarly enhanced sub-gap absorption in the LiI, NaI, and KI-treated films, suggesting that alkali metal cations could be more effective on passivating defects compared to  $\text{TMA}^+$  cations.

From the Tauc plots (Figure 2b), it was found that the (pseudo-direct) bandgap of  $\text{NaBiS}_2$  was slightly widened from 1.4 eV in the pristine film to 1.5 eV in all of the iodide-treated films. Furthermore, compared to the pristine film, the iodide-treated films also showed a significant change in their valence band density of states (VB DOS) profiles, which were determined by calculating the first derivative of the photoelectron yield  $Y$  (acquired from PYS measurements) with respect to the photon energy  $h\nu$  (see details in the Experimental Section), as displayed in Figure 2c. Note that 0 eV in the energy scale was set to coincide with the onset of the signal for the VB density of states for each sample, and the very weak signals above the VB maximum were mainly due to a magnification of the measurement noise during normalization. Nevertheless, the DOS profiles of all of the iodide-treated NC films were more or less similar to each other, suggesting that I 5p orbitals may dominate the upper VB states of the iodide-treated NC films, at least at the surface region (the information depth in our PYS measurements was estimated<sup>[17,18]</sup> to be below 10 nm). Herein, despite the surface-sensitivity of PYS technique, we would not expect to see a significant difference in the bulk region to the surface. This is because PYS technique could still probe through multiple NCs with small sizes ( $\approx 4.0 \pm 1.0$  nm), and it was also performed at atmospheric pressure

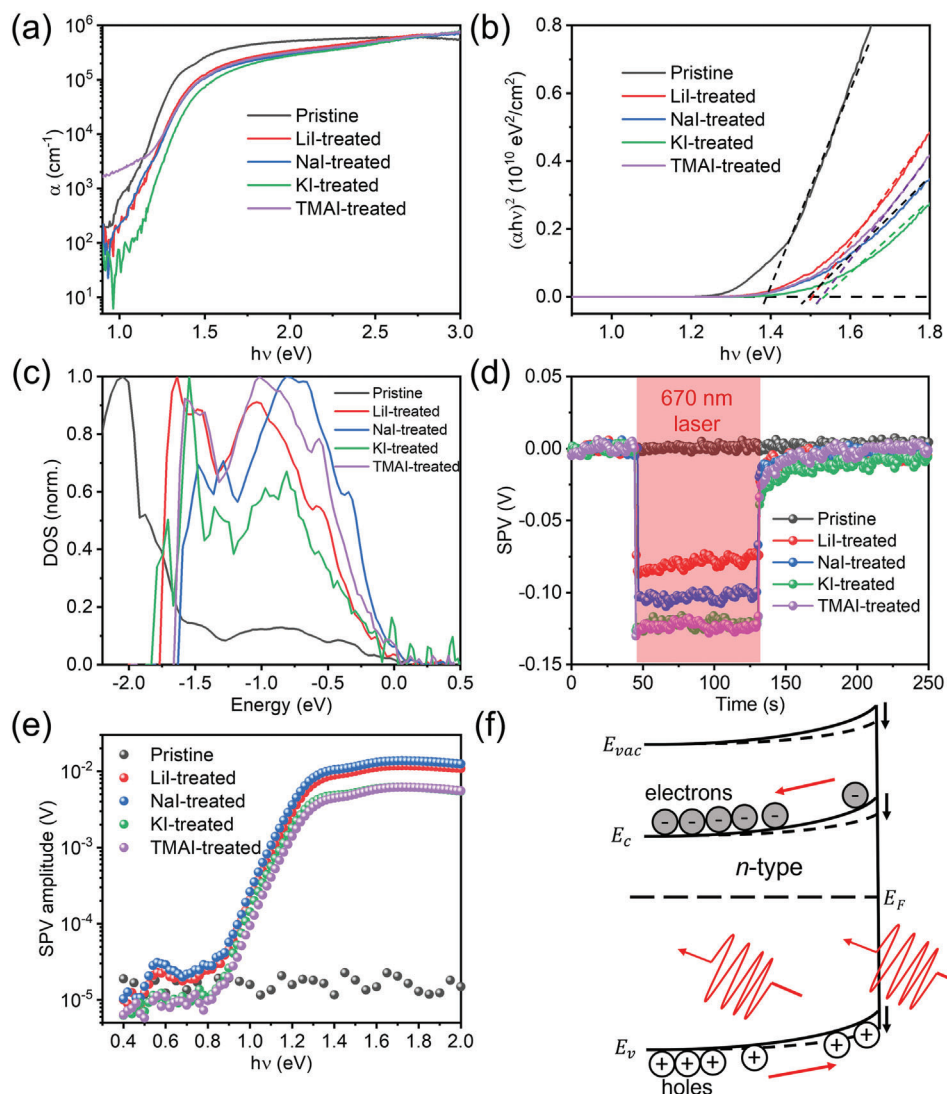


**Figure 2.** The effect of ligand exchange on the optoelectronic properties of NaBiS<sub>2</sub> nanocrystal (NC) films. a) Absorption coefficient spectra acquired from UV–Vis spectrophotometry and photothermal deflection spectroscopy (PDS) (details in the Experimental Section), and the associated b) Tauc plots. c) Normalized valence band density of states (VB DOS) obtained from photoelectron yield spectroscopy (PYS), d) steady-state surface photovoltage (SPV) under light illumination (670 nm wavelength cw laser), and e) modulated SPV amplitude as a function of different photon energies  $h\nu$  for the pristine and iodide-treated NaBiS<sub>2</sub> films. The peak near 0.6 eV  $h\nu$  is an artefact caused by stray light. In part (c), 0 eV is set to coincide with the onset of the VB density of states for each sample. f) An illustration of how the energy levels of iodide-treated NaBiS<sub>2</sub> NC films would be changed under light illumination, giving rise to a SPV signal.  $E_{vac}$ ,  $E_c$ ,  $E_F$ , and  $E_v$  refers to the vacuum, conduction, Fermi, and VB energy level, respectively. The pristine films were prepared by drop-casting, while the iodide-treated films were prepared by layer-by-layer (LBL) deposition up to a thickness of  $\sim 55$  nm.

to avoid any volatilization of Na species that could occur under ultra-high vacuum.<sup>[7]</sup>

To gain further understanding of spatial charge-carrier separation under open-circuit conditions, we performed steady-state surface photovoltage (SPV) measurements under illumination from a 670 nm wavelength continuous wave (cw) laser. This technique measures light-induced changes in the surface contact potential, which highly depends on the majority charge-carrier type and mobility. As shown in Figure 2d, we could clearly see negative responses from all of the iodide-treated samples, which reflects the process of the trapped surface electrons being neutralized by photo-induced holes drifting through the space-charge re-

gion, as illustrated in Figure 2f. This result therefore verifies the iodide-treated films to be *n*-type, which is consistent with that acquired from PYS and KP measurements (Figure S5, Supporting Information).

To further study sub-bandgap electronic transitions, light-modulated SPV spectroscopy, which could measure the SPV amplitude under different photon energies  $h\nu$ , were also performed.<sup>[19]</sup> This technique has a higher sensitivity than conventional steady-state SPV measurements owing to the combination of light modulation with lock-in detection, and could hence provide valuable information on charge-carrier separation upon light excitation. We can see from Figure 2e that all SPV signals

extend down to 0.8 eV, as confirmed from the measurements using a 1.13 eV long-pass filter (Figure S6a, Supporting Information). Note that the small peak at ~0.6 eV was simply an artefact caused by stray light. The sub-gap absorption at low photon energies suggests a wide distribution of defect states or S 3p states forming in different cation coordination environments, as shown in our previous work.<sup>[7]</sup> Interestingly, no detectable SPV signals in the pristine film were observed throughout the photon energy range from 0.4 to 2 eV, as displayed in Figure 2d,e. This absence of SPV signals in the pristine film could be due to two possible reasons: (1) intrinsically poor hole transport in the pristine film owing to its flat valence band edge,<sup>[7]</sup> and/or (2) poor inter-NC transport owing to the presence of long-chain organic ligands surrounding NCs. By contrast, strong SPV signals in all of the iodide-treated films indicate that after ligand exchange treatment, macroscopic charge-carrier transport within NaBiS<sub>2</sub> NC films has been indeed improved and hence the (average) separation distance between photogenerated charge-carriers could be also enlarged.<sup>[20]</sup> This improvement in macroscopic charge-carrier transport results mainly from the decreased distances between NCs when long-chain organic ligands have been replaced by short-chain iodide ligands, which facilitates the hopping of charge-carriers from one NC to another. In addition, the modulated SPV amplitudes were also found to be higher in thicker iodide-treated films (Figure S6b, Supporting Information), indicating that the detected SPV signals here were caused by charge-carrier transport from the NaBiS<sub>2</sub> bulk film toward the surface rather than the charge-carrier injection at the ITO/NaBiS<sub>2</sub> interface.

## 2.4. Charge-Carrier Dynamics in Iodide-Treated NaBiS<sub>2</sub> NC Films

To understand the kinetics of free charge-carriers, optical-pump-terahertz-probe (OPTP) measurements were performed on the pristine and iodide-treated NaBiS<sub>2</sub> films, as displayed in Figure 3a. This technique tracks the transient photoconductivity ( $\Delta\sigma$ ), which is determined by the product of charge-carrier densities  $n$  and mobilities  $\mu$ , of the samples excited by a pump beam. In our experiments, all of the samples were excited by a 400 nm wavelength pump beam, and the time evolution of  $\Delta\sigma$  ( $\Delta\sigma$  transients) was tracked from the transmitted terahertz beam at a specific time delay (see details in the Experimental section). Herein, the  $\Delta\sigma$  transients of all NaBiS<sub>2</sub> NC films could be fitted well by the two-level mobility model developed previously by Herz and co-workers.<sup>[21]</sup> This model accounts for the initially delocalized charge-carriers (with a delocalized mobility  $\mu_{del}$ ) quickly entering (at a localization rate  $k_{loc}$ ) into a localized state with a reduced mobility  $\mu_{loc}$ , subsequently followed by a slow relaxation process toward the ground state (at a recombination rate  $k_1$ ). Dividing  $\Delta\sigma$  by elementary charge  $q$  and the initial charge-carrier density after pump pulse excitation  $n_0$ , the OPTP transients can then be directly associated with the above parameters according to Equation 1.<sup>[21]</sup>

$$\frac{\Delta\sigma}{qn_0} = \left( \mu_{del} - \frac{\mu_{loc}k_{loc}}{k_{loc} - k_1} \right) e^{-k_{loc}t} + \frac{\mu_{loc}k_{loc}}{k_{loc} - k_1} e^{-k_1t} \quad (1)$$

The corresponding fitted curves based on the two-level mobility model are illustrated by the solid lines in Figure 3a, and

the fitted parameters are displayed in Table S1 (Supporting Information). According to ref. [22] the probing length  $L_p$ , which describes the average distance a charge-carrier moves over the half-period of the alternative electric field, can be estimated based on Equation 2.

$$L_p \approx \sqrt{\frac{6k_B T \mu}{\pi q f}} \quad (2)$$

where  $k_B$ ,  $T$ , and  $\mu$  refers to Boltzmann constant, temperature, probing frequency, and the sum mobility value ( $\frac{\Delta\sigma}{qn_0}$ ), respectively. From Figure 3a,  $L_p$  was found to be ~1.5 nm ( $\mu \approx 10^{-1} \text{ cm}^2 \text{ V}^{-1} \text{ s}^{-1}$ ) before 2 ps and ~0.4 nm ( $\mu \approx 3 \times 10^{-3} \text{ cm}^2 \text{ V}^{-1} \text{ s}^{-1}$ ) after 2 ps, both of which are smaller than the mean size of NaBiS<sub>2</sub> NCs ( $4.0 \pm 1.0$  nm), indicating that OPTP measurements are mainly probing intra-NC dynamics rather than inter-NC dynamics. Additionally, this result also implies that the sum mobility between NCs on length scales larger than one single NC could be even lower than  $10^{-3} \text{ cm}^2 \text{ V}^{-1} \text{ s}^{-1}$ .

As can be seen from Figure 3a, even though the early OPTP signals before 1 ps (dominated by delocalized charge-carriers) were enhanced by ~2–3 times after ligand exchange, the transients in all of the iodide-treated films still decayed substantially within 1 ps. This result is also consistent with the photo-induced absorption (PIA) transients (Figure 3b) extracted from short-time transient absorption (TA) spectra (Figure S7, Supporting Information). In these short-time TA measurements, the samples were first excited by a pump beam, and the changes in absorbance, arising from excited-state charge-carriers, could then be monitored by using a broad-band white light probe beam set at a specific time delay relative to the pump beam (pump-probe delay, see details in the Experimental section). Herein, all of the short-time TA spectra were acquired by exciting the samples with a 400 nm wavelength pump beam at  $33 \mu\text{J cm}^{-2} \text{ pulse}^{-1}$  fluence, and the PIA kinetics were extracted by averaging the signal intensities between 950 and 1000 nm wavelength, where the signal-to-noise ratio was the highest. We previously showed that the PIA transient of the pristine film is strongly correlated with the OPTP transient,<sup>[7]</sup> and the cause of PIA signals is possibly due to free electron transitions from the states near the conduction band minimum (CBM) to other higher excited states. Both OPTP and PIA transients hence indicate that the ultrafast charge-carrier localization process is still present in NaBiS<sub>2</sub> films even after ligand exchange treatment, which is also in good agreement with the analysis on the complex sum mobility spectra, as discussed in Note S1 (Supporting Information).

This ultrafast localization process has previously been shown to be associated with cation disorder in NaBiS<sub>2</sub> NCs, where small hole polarons form in Na<sup>+</sup>-rich clusters, while electrons are partially localized to Bi<sup>3+</sup>-rich clusters.<sup>[7]</sup> Therefore, the results here again suggest that the impact of cation inhomogeneity might be still significant in all of the iodide-treated NaBiS<sub>2</sub> films. Note that even though the surface of our NaBiS<sub>2</sub> films are Na-poor, the density of cation-rich clusters within the bulk film might be still high enough to localize most free charge-carriers.

Owing to the short probing length of the OPTP measurements, the higher  $\mu_{del}$  values in iodide-treated films were not directly caused by the improved inter-NC transport, but should

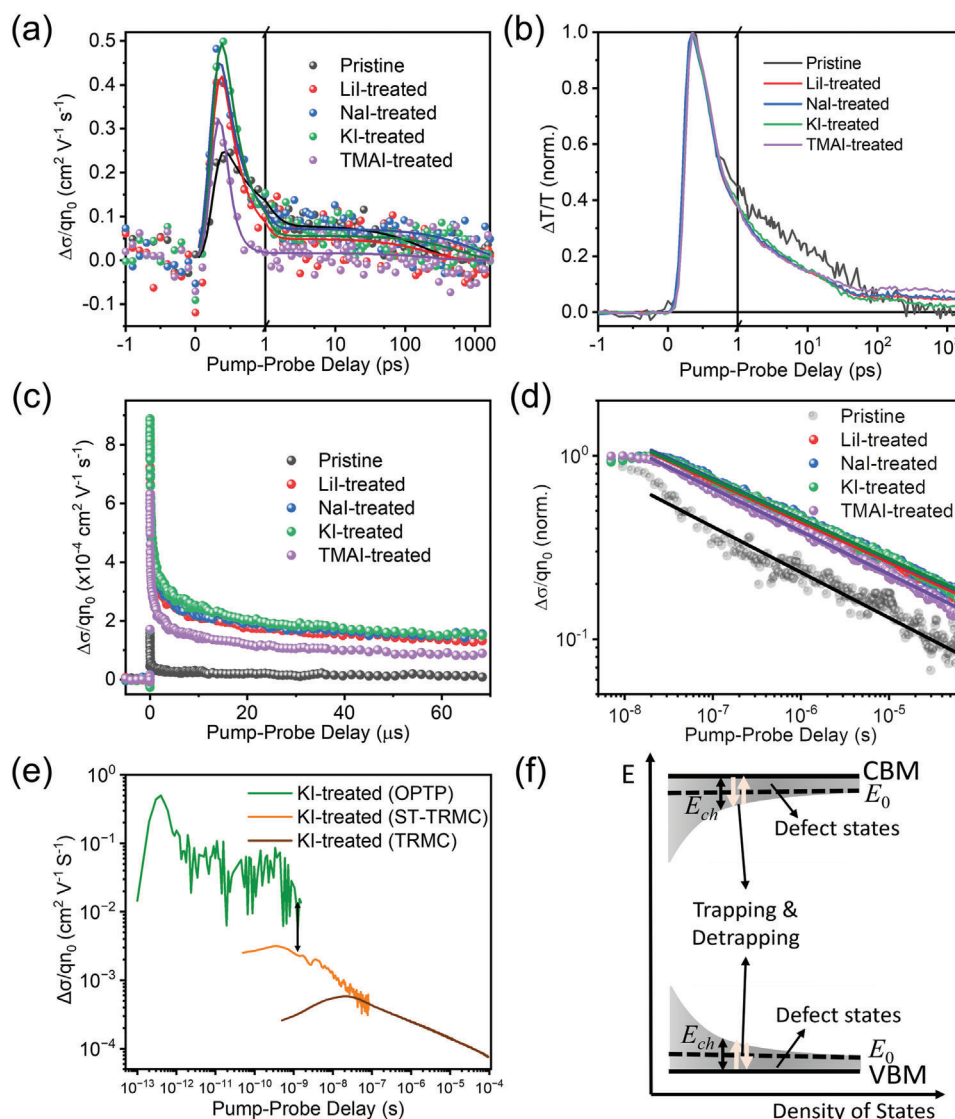


**Figure 3.** Charge-carrier dynamics of NaBiS<sub>2</sub> NC films. a) Optical-pump-terahertz-probe (OPTP) transients (probing frequency: 1 THz) of the pristine and iodide-treated NaBiS<sub>2</sub> films excited with 400 nm wavelength pump pulses at 4.6  $\mu$ J cm<sup>-2</sup> pulse<sup>-1</sup> fluence (pulse width:  $\sim$ 150 fs, repetition rate: 150 kHz).  $\Delta\sigma$ ,  $q$ , and  $n_0$  represent the photoconductivity, elementary charge, and initial charge-carrier density after the pump pulse excitation, respectively. b) The normalized photo-induced absorption (PIA) signal transients of the pristine and iodide-treated NaBiS<sub>2</sub> films excited by 400 nm wavelength pump pulses at 33  $\mu$ J cm<sup>-2</sup> pulse<sup>-1</sup> fluence (pulse width:  $\sim$ 100 ps, repetition rate: 1 kHz). All of the PIA transients were acquired by averaging the signals from 950 to 1000 nm wavelength in the short-time transient absorption (TA) spectra of the samples (Figure S6, Supporting Information). c) Time-resolved microwave conductivity (TRMC) transients (probing frequency: 9 GHz) of the pristine and iodide-treated NaBiS<sub>2</sub> films excited by 410 nm wavelength pump pulses (pulse width:  $\sim$ 5 ns, repetition rate: 50 Hz) at 0.51  $\mu$ J cm<sup>-2</sup> pulse<sup>-1</sup> fluence. d) The normalized TRMC transients (dots, normalized to the maximum values) of (c) and the fitted power-law curves (solid lines). e) Charge-carrier transients of the KI-treated NaBiS<sub>2</sub> film measured by OPTP, ST-TRMC (sample-terminated TRMC, see details in the Experimental Section), and TRMC on different time scales. f) Schematic of the multiple-trapping model. In our proposed model, the energy ( $E$ ) distribution of defect away from a mobility edge  $E_0$  is proportional to  $e^{-(E_0-E)/E_{ch}}$ , where  $E_{ch}$  is the characteristic band tail energy.

be attributed to the enhanced intra-NC transport, possibly due to the changes on their electronic band structure, as discussed in the previous section. On the other hand, the  $\mu_{loc}$  values were more or less similar in all of the NaBiS<sub>2</sub> films, suggesting that their final localized states for charge-carriers are likely very similar. As can be seen in Table S1 (Supporting Information), the higher  $\mu_{del}$  and similar  $\mu_{loc}$  values in the iodide-treated films eventually result in larger  $k_{loc}$  values. After being localized, all of the

charge-carriers then slowly relax to the ground state at a low rate  $k_1$  ( $\approx 10^{-3}$  ps<sup>-1</sup>), likely through non-radiative recombination pathways.

Since it is challenging to resolve the photoconductivity transients of NaBiS<sub>2</sub> films after 1 ns from OPTP measurements owing to the low signal-to-noise ratios, time-resolved microwave conductivity (TRMC) measurements were further employed. Similar to OPTP measurements, TRMC measurements can also

track the transient photoconductivity  $\Delta\sigma$  of the samples after pulsed pump excitation. In TRMC measurements, the samples were excited by a 410 nm wavelength pump beam, while the  $\Delta\sigma$  transients at a specific time delay were tracked using the microwave beam reflected from the samples placed in a resonance cavity. The resonance cavity was used for the build-up of a microwave standing wave in order to enhance the signals for the samples. Due to the use of this resonance cavity, TRMC measurements usually have a high sensitivity to very weak signals, while sacrificing their time resolution, which could only reach  $\sim 20$  ns. This technique is therefore useful to investigate the charge-carrier kinetics tail of NaBiS<sub>2</sub> extending to longer time scales than the time window in OPTP measurements (Figure 3c).

From Figure 3c, we can see that all iodide-treated NaBiS<sub>2</sub> films exhibited higher TRMC signals compared to the pristine film throughout the time window. In order to carefully compare the TRMC transients of different samples, we normalized the TRMC transients to their maximum values, and display the normalized transients in a log-log plot, as shown in Figure 3d. Owing to the low time resolution of the TRMC setup, we would only analyze the TRMC transients after a 20 ns pump-probe delay. Surprisingly, all of the normalized TRMC transients followed a power-law decay across 3 orders of magnitude in time scale (from tens of nanoseconds to tens of microseconds) and manifest as straight lines in the log-log plot (Figure 3d). This power-law decay has been found to occur in the multiple-trapping model, which is usually used to describe the multiple trapping/detrapping processes of charge-carriers caused by exponentially-distributed sub-gap defect states,<sup>[23–25]</sup> as illustrated in Figure 3f. These exponentially distributed defect states are also consistent with the SPV tails observed in Figure 2e, which extends down to 0.8 eV  $h\nu$ . In this model, only charge-carriers with an energy  $E$  exceeding the mobility edge  $E_0$  are assumed to be mobile and can contribute to the measured photoconductivity. Considering the charge-carriers with  $E \geq E_0$ , the TRMC transients of can be described by Equation 3.

$$\frac{\Delta\sigma}{qn_0} \propto t^{-\gamma} = t^{-(1-\frac{k_B T}{E_{ch}})} \quad (3)$$

In Equation 3,  $t$  is the pump-probe delay time, and  $\gamma$  is the exponent equal to  $1 - k_B T/E_{ch}$ .  $E_{ch}$  is the characteristic band tail energy. Based on this model, the defect density of states below  $E_0$  will be proportional to  $e^{-(E_0-E)/E_{ch}}$ , as shown in Figure 3f. We note that because the trapping/detrapping process could occur for both electrons and holes,  $E_{ch}$  is more likely an average parameter of the band tail energy below the CBM and above the VBM, as illustrated in Figure 3f. Since charge-carriers will essentially have been localized completely and formed polarons within the time window that TRMC measurements can resolve, the slow decays observed here most likely reflect the process for electron and hole polarons to diffuse slowly toward the same defect state and undergo non-radiative recombination. Neglecting the fast decay below the time resolution, the TRMC transients were found to be almost identical to the SPV transients (Figure S8, Supporting Information), verifying the very low recombination rates of separated charge-carriers via defects. More fluence-dependent results and analyses are also shown in Figure S9 (Supporting Information).

From the power-law fitting (solid lines in Figure 3d), the pristine film exhibited the largest  $\gamma$  value of  $0.25(\pm 0.002)$ , followed by  $0.23(\pm 0.001)$  in the TMAI-treated film. LiI-, NaI-, and KI-treated film showed a similar and smaller  $\gamma$  value of  $0.22(\pm 0.001)$ . These  $\gamma$  values are similar to those reported in  $\alpha$ -SnWO<sub>4</sub> and BaSnO<sub>3</sub>, where charge-carrier transport were also found to be limited by defects.<sup>[26,27]</sup> According to Equation 3, this result also indicates that the  $E_{ch}$  values, which reflects the steepness of band tailing or defect distributions, have become smaller in the iodide-treated films. This result hence suggests that despite the presence of an exponential tail of states extending from the band-edges, the deep-level traps might be passivated more by alkali cations than TMA<sup>+</sup> cations after ligand exchange treatment, which is again consistent with our conclusion made from Figure 2a.

In order to connect the charge-carrier dynamics from the picosecond to microsecond time scale, ST-TRMC (sample-terminated TRMC, see details in the Experimental Section) measurements were performed as well. By using a higher resonance microwave frequency ( $\sim 26$  GHz), shorter pump pulse width ( $\sim 80$  fs), and a detector with higher bandwidth, ST-TRMC measurements can reach a higher time resolution of  $\sim 1$  ns. Therefore, these measurements can effectively bridge the time scales between OPTP and conventional TRMC measurements.<sup>[28]</sup>

Figure S10 (Supporting Information) shows the ST-TRMC along with TRMC transients for the pristine and iodide-treated NaBiS<sub>2</sub> films, where we could see both transients to be connected smoothly for all of the samples. With the bridge of ST-TRMC transients, a complete set of information on charge-carrier transients spanning from 1 ps to 90  $\mu$ s for NaBiS<sub>2</sub> films can then be derived, with the KI-treated film as an example displayed in Figure 3f. We could clearly see an ultrafast localization process occurring within the first 1 ps, followed by a long kinetics tail extending from 1 ps up to 90  $\mu$ s. Surprisingly, there was a significant offset (black arrow in Figure 3f) between the OPTP- and TRMC-derived transients even at the same pump-probe delay. We do not believe that this offset is due to the larger probing regions for microwave pulses, since  $L_p$  was estimated to be  $\sim 1.3$  nm in our TRMC measurements (based on the  $\mu \approx 10^{-4}$  cm<sup>2</sup> V<sup>-1</sup> s<sup>-1</sup>) and is still in intra-NC length scale. On the other hand, this large offset was more likely caused by the strong frequency-dependence of sum mobilities when the NaBiS<sub>2</sub> films were probed at THz (OPTP) and GHz (TRMC) region, which was also observed in CuFeO<sub>2</sub> and BaSnO<sub>3</sub>.<sup>[22]</sup> As discussed in Note S1 (Supporting Information), the significant drop in sum mobilities at lower frequencies is also a result of charge-carrier localization based on the modified Drude-Smith model when  $c$  is close to 1. For comparison, some efficient bulk materials with very few localized charge-carriers such as silicon or 3D lead-halide perovskites have exhibited almost negligible offset between their OPTP- and TRMC-derived sum mobilities, as shown.<sup>[28]</sup>

## 2.5. Photovoltaic Performance of Ligand-Exchanged NaBiS<sub>2</sub> NC Films

With the insights into charge-carrier transport gained from the above spectroscopic studies, we further investigated whether an improvement in photovoltaic (PV) performance can be achieved

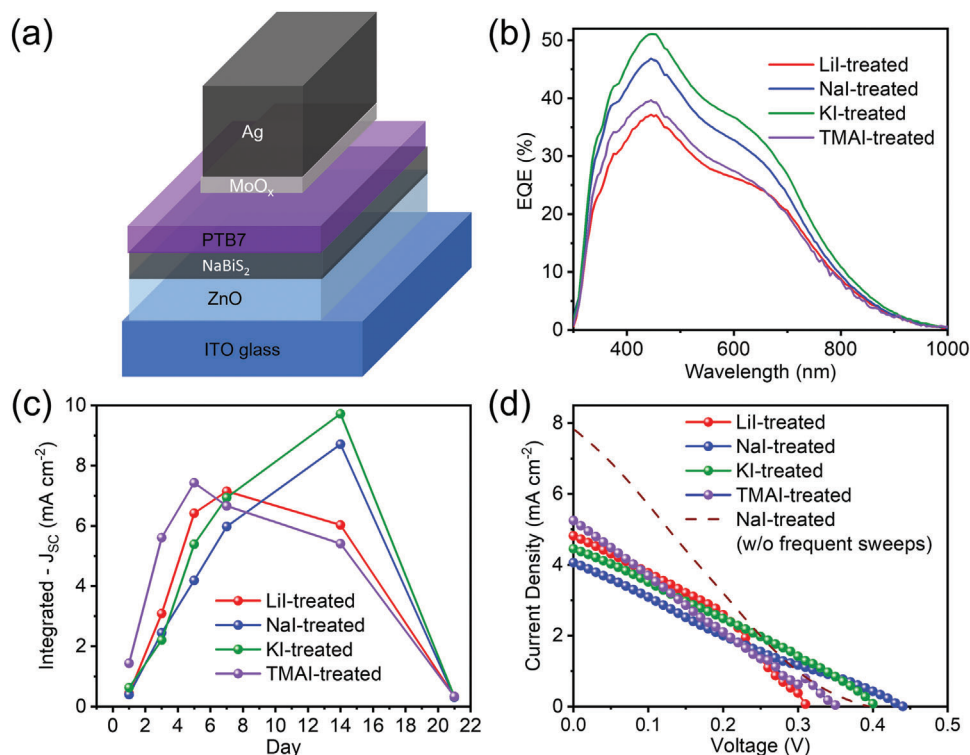


**Figure 4.** Photovoltaic (PV) performance of NaBiS<sub>2</sub> devices. a) PV device architecture adopted. b) External quantum efficiency (EQE) spectra with the highest short-circuit current density values (integrated- $J_{SC}$ , acquired from the integration of the product of EQE spectrum and AM 1.5G spectrum), c) evolution of the integrated- $J_{SC}$  values over time, and d) the current density-voltage ( $J$ - $V$ ) curves under AM 1.5G illumination (swept at a rate of 50 mV s<sup>-1</sup>) for champion iodide-treated NaBiS<sub>2</sub> PV devices. The dashed line shows the  $J$ - $V$  curve of the best NaI-treated NaBiS<sub>2</sub> PV device, obtained after storing in air for 3 weeks, during which no  $J$ - $V$  sweeps were performed. The  $J$ - $V$  curves of this champion device under forward and backward sweeps are shown in Figure S13 (Supporting Information).

in devices based on these iodide-treated NaBiS<sub>2</sub> films. Herein, ZnO and PTB7/MoO<sub>x</sub> were found to be the most effective electron transport layer (ETL) and hole transport layer (HTL), respectively. The architecture of NaBiS<sub>2</sub> devices is illustrated in Figure 4a, and the film morphology on top of the ZnO layer was optimized by using toluene as the solvent. As can be seen in the atomic force microscopy (AFM) images (Figure S1, Supporting Information), films treated by different iodides all had a compact morphology. Although some “wrinkle patterns”, possibly caused by residual film stress,<sup>[29]</sup> were seen in the LiI- and NaI-treated films, the root-mean-square roughness of all films was below 5 nm (the specific values are noted in the caption of Figure S1, Supporting Information).

The best PV performance was achieved in devices fabricated based on 3 layers of NaBiS<sub>2</sub> NCs (Figure S11a, Supporting Information), with a film thickness of 55±4 nm, as determined from cross-sectional scanning electron microscopy (SEM) measurements (Figure S11b, Supporting Information). As displayed in Figure 4b, the optimized NaBiS<sub>2</sub> devices treated by different iodides could all exhibit external quantum efficiency (EQE) values over 20% in the visible wavelength range, and the KI-treated device even showed an EQE value over 50% near 450 nm wavelength. It can be seen that the EQE values tend to be higher at shorter wavelengths, which might result from the stronger absorption or more efficient charge-carrier extraction near the ZnO layer (light illumination side). Integrating the measured EQE val-

ues across the 1-sun AM 1.5G spectrum gives the short-circuit current density (integrated- $J_{SC}$ ) values of 7.15, 8.71, 9.72, 7.43 mA cm<sup>-2</sup> for the best LiI-, NaI-, KI-, and TMAI-treated devices, respectively. In addition, using the spectroscopic limited maximum efficiency (SLME) model developed previously,<sup>[7,30]</sup> the limit in short-circuit current density ( $J_{SC}^{SLME}$ ) can also be estimated. In the SLME model, the internal quantum efficiency (IQE) is taken as unity above the bandgap, such that the EQE spectra follows the measured absorption spectra of the samples. We could hence calculate the  $J_{SC}^{SLME}$  values for different iodide-treated films based on their absorption coefficient spectra at an optimal thickness of 55 nm, as displayed in Table S2 (Supporting Information). It can be seen that these calculated  $J_{SC}^{SLME}$  values far exceed the corresponding integrated- $J_{SC}$  values obtained from the measured EQE spectra, which suggests that most photo-excited charge-carriers could not be effectively extracted out of the NaBiS<sub>2</sub> devices.

It is also worth mentioning that these peak integrated- $J_{SC}$  values could only be reached after aging the devices in ambient air for 1–2 weeks under low-level standard laboratory lighting (Figure 4c), while the as-made devices had EQE values that were barely measurable. This long-term aging process has also been reported in AgBiS<sub>2</sub> devices<sup>[5,15]</sup> and was attributed to a lowering of the hole extraction level of MoO<sub>x</sub> when oxidized in air.<sup>[31]</sup>

The PV performance of different iodide-treated NaBiS<sub>2</sub> devices were characterized by current density-voltage ( $J$ - $V$ ) sweeps (Figure 4d) with the extracted parameters listed in Table S3

(Supporting Information). We can see that these NaBiS<sub>2</sub> devices exhibited power conversion efficiencies (PCEs) of  $\approx 0.4$ – $0.5\%$ , which is almost an order of magnitude larger than the highest PCE reported in the literature so far ( $0.07\%$ ).<sup>[14]</sup> We also note that the best device previously reported had NaBiS<sub>2</sub> NCs mixed with PbX<sub>2</sub> (X = Br, I), which does not address the toxicity issue of lead-halide perovskites, whereas no lead-based compounds were included in our fabricated PV devices. The main improvement came from the much higher  $J_{SC}$  values ( $4$ – $5\text{ mA cm}^{-2}$ ) of our devices compared to the previously reported value ( $0.18\text{ mA cm}^{-2}$ ), which may be due to the significantly enhanced charge-carrier transport in our devices. Nevertheless, the measured fill-factor (FF) values were still low ( $< 35\%$ ), and the open-circuit voltage ( $V_{OC}$ ) values were only between  $0.3$  to  $0.4\text{ V}$ , which are almost one third of the limit value calculated from the SLME model ( $V_{OC}^{SLME}$ , Table S2, Supporting Information). As a result, the PCEs of our optimized NaBiS<sub>2</sub> devices were still far below their expected SLME values (Table S2, Supporting Information).

Frequent  $J$ – $V$  sweeps were also found to affect NaBiS<sub>2</sub> device performance, making a statistical evaluation on device performance challenging. As can be seen in Figure 4c, the integrated- $J_{SC}$  values for all the NaBiS<sub>2</sub> devices under frequent  $J$ – $V$  sweeps dropped dramatically after 3 weeks. On the other hand, the devices without any  $J$ – $V$  sweeps could retain their EQE values after storing in air for 36 days (Figure S12, Supporting Information). This result suggests that NaBiS<sub>2</sub> devices themselves are stable in air, but could be substantially damaged after applying an electric field. For comparison, a  $J$ – $V$  sweep was performed on the device stored in air for 3 weeks, during which no extra  $J$ – $V$  measurements were conducted to avoid device damage. As a result, a PCE of  $0.74\%$  along with a  $J_{SC}$  of  $7.73\text{ mA cm}^{-2}$  and  $V_{OC}$  of  $0.39\text{ V}$  could be achieved in a NaI-treated device (the dashed line in Figure 4d). This PCE value is over an order of magnitude higher the previous record, and clearly indicates that NaBiS<sub>2</sub> devices without frequent  $J$ – $V$  sweeps are indeed more likely to exhibit better performance. We note that although the highest EQE value was seen in the device based on the KI-treated film, which also has the highest measured sum mobilities among out of all of the iodide-treated films, the highest PCE value was not recorded in the KI-treated device. Actually, none of the PV parameters acquired from  $J$ – $V$  sweeps correlated directly with the trends in OPTP or TRMC kinetics. This surprising result, along with the significant change in PV performance after conducting frequent  $J$ – $V$  sweeps, further motivates us to investigate factors limiting device performance in more detail, which will be discussed in the next section.

## 2.6. Device Loss Analysis and Ion Migration in NaBiS<sub>2</sub> NC Films

The large  $V_{OC}$  deficit ( $\approx 0.7$ – $0.8\text{ V}$ ) between our extracted values and the SLME limit ( $V_{OC}^{SLME}$ , Table S2, Supporting Information) might be intuitively assumed to be due to more defects introduced during ligand exchange treatment. However, the TMAI-treated device would then be expected to show the lowest  $V_{OC}$  value, owing to the most defects being introduced among all of the iodide-treated films (Figure 2a), which was not the case. Moreover, charge-carrier kinetics were found to be almost independent

of defect densities in our previous work.<sup>[7]</sup> Therefore, we suspect ion migration to be a hidden factor that limits the performance of NaBiS<sub>2</sub> devices based on the two observations below.

First, NaBiS<sub>2</sub> devices showed significant hysteresis in their  $J$ – $V$  curves when swept in opposite directions (Figure 5a), which is also common in perovskite solar cells where halide anions or A-site cations could easily migrate under bias.<sup>[32–34]</sup> Second, the  $V_{OC}$  of the NaBiS<sub>2</sub> device would drop rapidly under continuous 1-sun illumination. Quasi-Fermi level splitting (i.e.,  $V_{OC}$ ) within a PV device, which can be monitored by a Source Measure Unit (SMU) set on zero current mode, should have remained constant under continuous light illumination. However, if ions also migrate under applied bias and accumulate at the interfaces between NaBiS<sub>2</sub> and the transport layers, a large excess charge-carrier gradient might be induced in the vicinity of the interface, which could introduce extra interface recombination and hence reduce the quasi-Fermi level splitting.<sup>[35,36]</sup> We can see from Figure 5b that there is indeed a reduction in the  $V_{OC}$  of the LiI-treated NaBiS<sub>2</sub> device under continuous light illumination, dropping from  $0.31\text{ V}$  to almost  $0\text{ V}$  after only  $100\text{ s}$  at open-circuit. For reference, the  $V_{OC}$  evolution of a typical AgBiS<sub>2</sub> device under the same experimental conditions was also recorded, which only dropped by approximately  $10\text{ meV}$  during the same period, as displayed by the black dots in Figure 5b. This can be explained by more facile ion migration in NaBiS<sub>2</sub> devices compared to in AgBiS<sub>2</sub> devices. From our present study, it is difficult to identify the ionic species migrating, but we suggest Na<sup>+</sup> to be a potential source since (1) Na<sup>+</sup> is light and has been shown to be very mobile in batteries, and (2) the most favorable defects in NaBiS<sub>2</sub> are Na vacancies, which could mediate Na<sup>+</sup> migration more easily.

An insight from these results is that apart from strong charge-carrier localization, accumulated ions could also impede the charge-carrier extraction in NaBiS<sub>2</sub> PV devices. If the migrated ions are trapped at the absorber/transport layer interfaces and could not relax to their original positions when the applied bias vanishes, the PV devices would then show significantly reduced  $V_{OC}$  values and could no longer function normally, as shown in Figure S14a,b (Supporting Information). Therefore, the rapid decrease in the PV performance of NaBiS<sub>2</sub> PV devices under frequent  $J$ – $V$  sweeps could be potentially associated with facile ion migration in these devices.

In order to quantify how easily ions could migrate in NaBiS<sub>2</sub> devices, temperature-dependent transient current measurements were performed. Herein, the electron-only NaBiS<sub>2</sub> device with the architecture ITO/ZnO/(NaI-treated) NaBiS<sub>2</sub>/PCBM/Ag was used to simplify the analysis. Herein, the NaI-treated film was used in order to exclude any contributions from other cations. The transient current densities of the electron only NaBiS<sub>2</sub> device at temperatures from  $270$  to  $360\text{ K}$  are shown in Figure 5c. The current density transients  $J(t)$  could be fitted with a mono-exponential model  $J(t) = J_0 + Ae^{-K_1 t}$ , with  $J_0$  the saturation current density and  $K_1$  the decay rate proportional to ion conductivity. The fitted parameters for the current density transients at different temperatures are displayed in Table S4 (Supporting Information), where we could see an overall trend of larger  $K_1$  and smaller  $J_0$  values at higher temperatures. These results could be understood by the stronger screening effect on the applied bias when more ions are thermally activated and accumulated at higher temperatures. Based on the fitted  $K_1$  values at

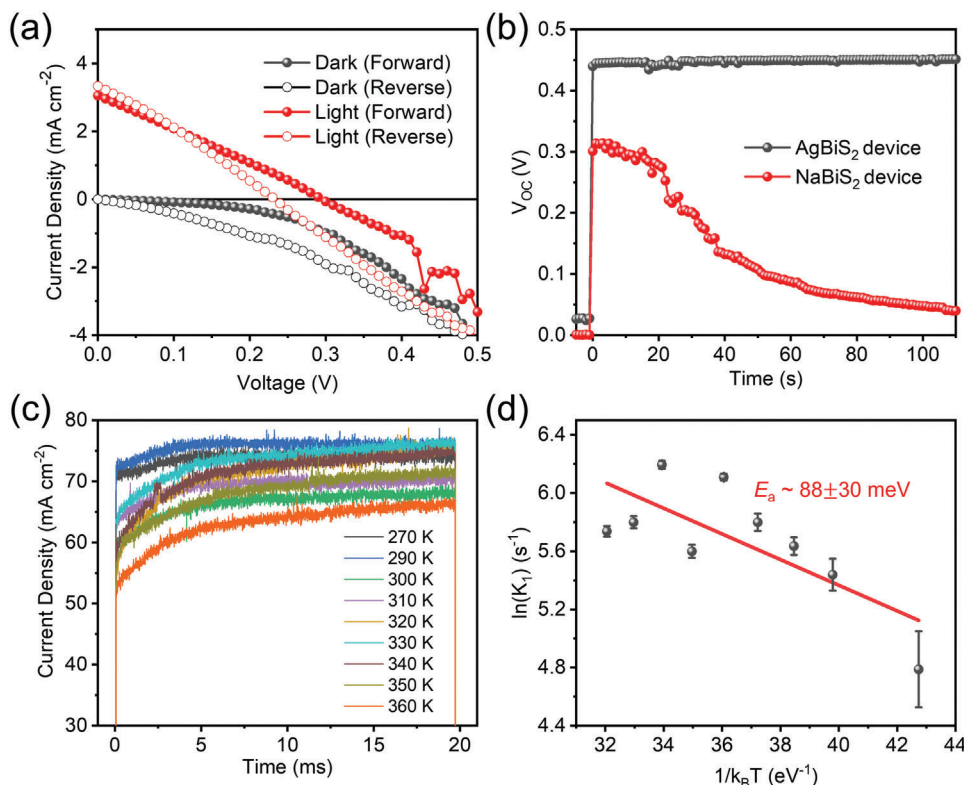


**Figure 5.** Ion migration in NaBiS<sub>2</sub> devices. a) The current density-voltage ( $J$ - $V$ ) curves measured at forward (0 to 0.5 V) and reverse (0.5 to 0 V) scan directions for a LiI-treated NaBiS<sub>2</sub> device. Both the measurements performed in the dark and under AM 1.5G illumination are displayed. b) Evolution in the open-circuit voltage ( $V_{OC}$ ) of AgBiS<sub>2</sub> and NaBiS<sub>2</sub> devices under continuous 1-sun illumination over time. Fresh devices were measured in both cases, with no prior  $J$ - $V$  sweeps. c) Transient currents of the electron-only NaBiS<sub>2</sub> device at different temperatures. The electron-only device has an architecture of ITO/ZnO/NaI-treated NaBiS<sub>2</sub>/PCBM/Ag. The voltage amplitude, pulse duration, and pulse frequency used during transient current measurements were 2.5 V, 20 ms, and 1 Hz, respectively. d) The Arrhenius plot extracted from part (c). Here,  $\ln(K_1)$  represents the natural logarithm of the exponential decay rate  $K_1$  when the transient currents approached the saturation current density. An activation energy barrier  $E_a$  of  $88 \pm 30$  meV was extracted from the slope of the Arrhenius plot.  $k_B$  and  $T$  refers to Boltzmann constant and temperature, respectively.

different temperatures  $T$ , an Arrhenius plot depicting the correlation of  $\ln(K_1)$  with  $1/k_B T$  can be acquired, as shown in Figure 5d. The activation energy barrier  $E_a$ , which corresponds to the barrier to be overcome for ion migration, could then be extracted from the slope of  $\ln(K_1)$  in the Arrhenius plot. We note that although the poor conductivity and strong scattering between NCs might introduce more scatter in the data, as previously observed for double perovskites<sup>[37,38]</sup> and AgBiS<sub>2</sub> NCs,<sup>[39]</sup> we could still see a negative correlation between  $\ln(K_1)$  and  $1/k_B T$ , which allows us to estimate an  $E_a$  value for NaBiS<sub>2</sub> to only be  $88 \pm 30$  meV. This value is even lower than those reported in lead-halide perovskites (LHPs) ( $E_a \approx 120$  to 600 meV),<sup>[32,40]</sup> where obvious ion migration has been already observed. We hence conclude here that the performance of NaBiS<sub>2</sub> devices might be also greatly limited by the severe ion migration.

Thus, in order for NaBiS<sub>2</sub> PVs to approach the optical limits in performance, ion migration is undoubtedly a pressing issue to be addressed, and the strategies developed for LHPs such as composition tuning or additive introduction, might apply to NaBiS<sub>2</sub> NCs as well. On the other hand, NaBiS<sub>2</sub> is revealed as a mixed electronic/ionic conductor where the conduction is highly associated with the voltage sweep history, and could therefore be particularly useful in applications requiring ionic conductors,

such as memristors used in neuromorphic computing,<sup>[41,42]</sup> or conductive membranes applied in fuel cells and batteries.<sup>[43,44]</sup>

### 3. Conclusion

This work found that iodide salts, including LiI, NaI, KI, and TMAI can effectively replace the long-chain organic ligands used during NaBiS<sub>2</sub> NC synthesis to give rise to compact thin films. As verified from OPTP, TRMC, and SPV measurements, ligand exchange led to an enhancement in charge-carrier transport over both the local and macroscopic length scales. The enhancement in macroscopic mobility could be due to the NCs becoming closer together, such that charge-carriers could more easily hop in between, while the enhancement in local intra-NC mobility indicates that ligand exchange could also alter the electronic band structure of individual NaBiS<sub>2</sub> NCs, possibly via iodide or cation incorporation. During ligand exchange treatment, extra defects may have been introduced, but these were passivated by the alkali cations from the inorganic ligands used, as seen from the sub-bandgap absorption measurements (Figure 2a) and TRMC kinetics (Figure 3d). Surprisingly, despite the enhanced mobilities, ultrafast localization is still present in all of the

iodide-treated films, suggesting that cation inhomogeneity cannot be greatly improved following ligand exchange. Nevertheless, the high absorption coefficients of NaBiS<sub>2</sub> enable the fabrication of ultrathin PV devices, where the impact of poor charge-carrier transport could be mitigated. Our optimized NaBiS<sub>2</sub> PV devices, with 55 nm thick absorber layers, exhibit decent EQEs peaking at over 50%, and have champion PCEs an order of magnitude higher than the previous record. Apart from charge-carrier localization, temperature-dependent transient current measurements also unveil facile ion migration to be another limiting factor for NaBiS<sub>2</sub> PVs. This factor could lead to the observed reduction in  $V_{OC}$  under continuous operation, as well as a significant dependence of the measured PCEs on the  $J$ - $V$  sweep history. Thus, for NaBiS<sub>2</sub>, general approaches taken to optimize NC absorbers, such as by adjusting film thickness, are very unlikely to achieve higher PCEs. Instead, developing methods to suppress ion migration will be critical. On the other hand, although this strong ionic conductivity is detrimental for PV devices, it could be useful in applications requiring ionic conductors, including neuromorphic computing<sup>[41,42]</sup> and energy storage,<sup>[43,44]</sup> which open up a different direction of research for this novel material.

## 4. Experimental Section

**Synthesis of NaBiS<sub>2</sub> NCs:** NaH (10 mg, dry, 90%, Merck), 132 mg triphenyl bismuth (99%, Alfa Aesar) and 32 mg sulfur powder (99.5%, Alfa Aesar) were dissolved in 10 mL degassed OLA (70%, Merck) under stirring at room temperature for 15 min. The solution was heated at 80 or 150 °C for 30 min depending on the desired size of the NCs. All the above processes were performed in an Ar-filled glovebox. Later, the whole solution was cooled down to room temperature in a water bath, and mixed with 6 mL hexane (> 95%, Merck) and 14 mL OA (90%, Merck). The mixed solution was stirred for at least 2 h to replace the original oleylamine ligands with the more strongly-coordinating oleic acid ligands. Next, the solution was equally divided between four centrifuge tubes (7.5 mL for each). In the first purification process, 7.5 mL ethyl acetate (anhydrous, > 99.9%, ROMIL) and 7.5 mL acetone (anhydrous, > 99.9%, ROMIL) were added into each tube containing the solution and centrifuged at 7000 rpm for 3 min. The precipitated NCs were re-dispersed in 12 mL toluene and equally divided into 2 centrifuge tubes (6 mL for each). In the second purification process, 3 mL ethyl acetate and 3 mL acetonitrile (anhydrous, > 99.9%, ROMIL) were added into each tube containing the solution and centrifuged again at 7000 rpm for 3 min. The precipitated NCs were re-dispersed in toluene, and the solution was filtered by a 0.22 μm PTFE syringe filter. The final concentration of the NaBiS<sub>2</sub> NC solution was 20 mg mL<sup>-1</sup>. Due to the absence of the ν(NH<sub>2</sub>) stretching mode at ≈3300 cm<sup>-1</sup> in the FTIR spectrum of the NaBiS<sub>2</sub> NC film (see Figure 1a), it was concluded that most organic ligands attaching to NaBiS<sub>2</sub> NCs were OA rather than OLA ligands.<sup>[14]</sup>

**Optoelectronic Characterizations:** The UV–Vis spectrophotometry absorption spectra were measured in a Shimadzu UV 3600 spectrometer equipped with an integrating sphere. For PDS measurements, NC films were drop-cast on Spectrosil 2000 quartz substrates and immersed in an inert liquid FC-72 Fluorinert (3 M Company), which has a high thermo-optic coefficient. A monochromatic beam from a 250 W quartz tungsten halogen lamp (Newport) integrated with a 250 mm focal length monochromator (CVI DK240) was illuminated perpendicularly to the sample surface, modulated with a mechanical chopper at a frequency of 13 Hz. Non-radiative recombination processes at the film surface led to a temperature gradient, and hence a refractive index gradient in the liquid surrounding the sample. A 670 nm cw diode laser beam parallel to the sample surface (transverse configuration) was deflected as a result of the refractive index modulation in the liquid and detected by a quadrant photodiode,

with the signal amplitude demodulated with a lock-in amplifier (Stanford Research Systems SR830). For FTIR measurements, NC films were spin-coated on CRYSTRAN CaF<sub>2</sub> substrates, and the FTIR spectra were collected on a Bruker Vertex 70 V instrument using a DLATGS (deuterated L-alanine doped triglycine sulfate) detector under transmission mode. The absorption coefficient  $\alpha$  was calculated based on Equation 4.

$$\alpha = \frac{\ln\left(\frac{1-R}{T}\right)}{d} \quad (4)$$

In Equation 4,  $R$ ,  $T$ , and  $d$  refers to the reflectance, transmittance, and film thickness of the sample. Herein,  $R$  and  $T$  were measured by the UV–Vis with an integration sphere, and  $d$  was determined from an atomic force microscopy (Nanoscope III). To acquire more precise  $\alpha$  spectra, the relative absorption spectra measured by PDS were mapped to the absolute  $\alpha$  spectra determined by UV–Vis at 3 eV.

For TA measurements, the second harmonic (400 nm) of the Ti:Sapphire laser provided ≈100 fs pump pulses. Broad-band NIR probe pulses ranging from 830 to 1000 nm were provided by a noncollinear optical parametric amplifier (NOPA) setup. Probe pulses were split into two beams by a beam splitter. The other reference beam was used to calibrate shot-to-shot noise coming from the NOPA setup itself. Both the probe and reference beams were detected by a Si dual-line array detector read out by a custom-built board from Stresing Entwicklungsbüro. The transmittance with and without pump excitation ( $T_{\text{pump on}}$  and  $T_{\text{pump off}}$ ) were collected alternatively at a repetition rate of 500 Hz, and the TA signals were expressed as  $\frac{\Delta T}{T} = \frac{T_{\text{pump on}} - T_{\text{pump off}}}{T_{\text{pump off}}}$ .

Optical-pump-Terahertz-probe (OPTP) measurements enable the monitoring of transient photoconductivity by detecting the change in terahertz transmission ( $\Delta T$ ) after excitation the samples with a 400 nm wavelength pump pulse. A mechanical delay stage is employed to investigate a time window of 1.6 ns. The measured  $\Delta T$  is corrected for the terahertz generation originating from the sample, which may occur during photoexcitation. To determine the photoconductivity spectrum, the transmitted terahertz beam was sampled using a second delay stage. The time-domain signals  $T(t)$  and  $\Delta T(t)$  underwent Fourier transformation to obtain the frequency-domain signals  $T(\omega)$  and  $\Delta T(\omega)$ . Employing the thin-film approximation, it becomes possible to derive the frequency-dependent sheet photoconductivity  $\Delta\sigma(\omega)$ . This parameter was connected to the sum of electron mobility and hole mobility  $\mu_{\Sigma}(\omega)$  in the material, as shown in Equation 5.

$$\Delta\sigma(\omega) = q\phi\mu_{\Sigma}n_0 = -\varepsilon_0c(1+n_{\text{sub}})\frac{\frac{\Delta T}{T}}{1+\frac{\Delta T}{T}} \quad (5)$$

In Equation 5,  $\varepsilon_0$  is the vacuum permittivity,  $c$  the speed of light,  $n_{\text{sub}}$  the refractive index of the substrate ( $n_{\text{quartz}} = 2$ ) and  $n_0$  the initial pump-induced sheet charge-carrier density.  $n_0$  depends on pump power density ( $I_p = 1.4 \text{ W cm}^{-2}$ ), the photon energy ( $E_{ph} = 3.1 \text{ eV}$ ), the laser repetition rate ( $r_{rep} = 150 \text{ kHz}$ ) and the absorbance ( $A$ ), determined by UV–Vis spectroscopy and calculated according to  $n_0 = AI_p/E_{ph}r_{rep}$ .

The measurements of cavity-based time-resolved microwave conductivity (TRMC) rely on the interaction between the electric field component of a microwave and the mobile charge-carriers present in the material being probed, which leads to variations in both phase and/or amplitude directly influenced by changes in conductance. The microwaves used in the experiment are generated using a voltage-controlled oscillator (Sivers IMA VO3262X) and are directed onto the sample through waveguides. To enhance the signal amplitude, the sample is placed within a cavity that allows for resonant condition. For optical excitation, a 50 Hz pump laser based on a wavelength-tunable optical parametric oscillator (OPO) set to 410 nm and a pulse width of ≈ 5 ns was used. The samples are excited with varying photon numbers between  $I_0 \approx 1 \times 10^{12}$  and  $7 \times 10^{14}$  photons

pulse<sup>-1</sup> cm<sup>-2</sup>. In the TRMC measurements, the photoconductivity  $\Delta\sigma$  is determined from the measured quantities according to Equation 6.

$$\Delta\sigma = \frac{\frac{-\Delta P}{P}}{K} = \frac{\left(\frac{-\Delta V}{V_{det}}\right)g m}{K} \quad (6)$$

In Equation 6,  $\Delta V$  is the raw signals measured at the detector and is related to the voltage difference relative to the detector voltage  $V_{det} \approx 680$  mV via the electrical amplification gain factor  $g = 3.27 \times 10^{-2}$ .  $m \approx 2.1$  is the power correlation factor for the relative microwave power  $\Delta P/P$ .  $K$  is the sensitivity factor of the cavity, which was found to be  $\approx 45,000$  m S<sup>-1</sup> for low conductivity thin films on non-conductive quartz substrates with 1 mm thickness. Details on the impedance model used are found in the earlier work.<sup>[28]</sup> In addition, a sample-terminated TRMC setup (ST-TRMC) setup was used in order to improve the time resolution. It works at 26–40 GHz, uses faster detection electronics (RTO2044 Oscilloscope, 20 Giga sample per second, bandwidth of 4 GHz) and a femtosecond laser as the excitation source (repetition rate: 150 kHz, pulse width: 70 fs, and wavelength: 400 nm). More details are found elsewhere.<sup>[28]</sup>

Kelvin probe (KP) and photoelectron yield spectroscopy (PYS) were combined to measure the work function ( $\Phi$ ) and ionization potential ( $E_i$ ), respectively, of the prepared thin films by employing a KP Technology SKP5050-APS02 setup in an N<sub>2</sub>-filled environment.<sup>[18]</sup> The KP system uses a 2.0 mm diameter tip with a gold alloy coating which is calibrated on a gold reference sample. The KP was placed in a Faraday cage which screens the external electrical fields.

The work function was determined by measuring the contact potential difference (CPD) between the Kelvin probe (reference electrode) with a known work function,  $\Phi_{tip}$ , and the investigated thin film. The CPD is measured with a resolution of 3 mV. Since  $\Phi_{tip}$  is known from reference measurements on an Au thin film, the work function of the sample,  $\Phi_{sample}$ , is calculated from Equation 7.

$$\Phi_{sample} = \Phi_{tip} + q \cdot \text{CPD} \quad (7)$$

In Equation 7  $q$  is the elementary charge. The steady-state surface photovoltage (SPV) was acquired by comparing the CPD under light illumination (CPD<sub>light</sub>) and at dark (CPD<sub>dark</sub>), as shown in Equation 8.

$$\text{SPV} = \text{CPD}_{\text{light}} - \text{CPD}_{\text{dark}} \quad (8)$$

The light source used in the experiments was 670 nm cw laser at an intensity of  $\approx 100$  mW cm<sup>-2</sup>.

The PYS setup uses the same Kelvin probe to detect the photoemission currents as a function of incident photon energy. The light source comprises of a deuterium (D<sub>2</sub>) lamp coupled with a grating monochromator. The range of the incident photon energy was 3.4–7.5 eV. The sample was illuminated via a DUV optical fiber.

The ionization potential,  $E_i$ , of samples was determined by measuring the photoelectron yield  $Y(h\nu)$  as a function of photon energy  $h\nu$ .  $Y(h\nu)$  is defined as the number of photoemitted electrons per incident photon at a given photon energy  $h\nu$ . By extrapolating the linear part of the  $Y^{1/3}(h\nu)-h\nu$  plot to x-axis, the ionization potential is found according to Equation 9.

$$Y(h\nu) \propto (h\nu - E_i)^3 \quad (9)$$

Measurements were conducted with a step of 1 nm and the photoemission threshold is determined with a resolution of 30 meV.

The electron affinity (EA), i.e., conduction band minimum (CBM) referred to the local vacuum level is calculated from Equation 10.

$$EA = E_{\text{CBM}} = E_i - E_g \quad (10)$$

In Equation 10,  $E_g$  is the thin film (surface) bandgap. On the other hand, the  $E_{\text{VBM}}$  and  $E_{\text{CBM}}$  is determined from Equations 11 and 12, respectively.

$$E_{\text{VBM}} = \Phi - E_i \quad (11)$$

$$E_{\text{CBM}} = (\Phi - E_i) + E_g \quad (12)$$

Further details on the KP-PYS setup and the applied methodology of evaluating the experimental data can be found elsewhere.<sup>[18]</sup>

Total density of states (DOS) spectra spreading from  $E_F$  down to  $h\nu-\Phi$  could be obtained from the  $Y(h\nu)-h\nu$  plots.<sup>[45]</sup> Since the total DOS extending from  $E_F$  down to  $h\nu-\Phi$  is proportional to the total  $Y(h\nu)$ , the first derivative of  $Y(h\nu)$  with respect to  $h\nu$  provides the DOS at a specific  $h\nu$  value. Therefore, the overall DOS profile extending from  $E_F$  down to  $h\nu-\Phi$  could be displayed as  $dY/dh\nu(h\nu)$ .

Optically-modulated SPV spectra were measured in an ambient atmosphere in a parallel plate capacitor configuration, composed of a quartz cylinder partially coated with the SnO<sub>2</sub>:F electrode and a mica sheet as an insulator.<sup>[46]</sup> The SPV signal is defined as the change in the surface potential as a result of the illumination. Front illumination (light impinging the surface) was provided by a halogen lamp, coupled to a quartz prism monochromator (SPM2), and modulated at a frequency of 8 Hz by using an optical chopper. In-phase and 90° phase-shifted SPV signals were detected with a high-impedance buffer and a dual phase lock-in amplifier (EG&G 5210). The amplitude of the optically modulated SPV signal is defined as the square root of the sum of the squared in-phase and 90° phase-shifted SPV signals.

Transient SPV measurements were performed using an oscilloscope card (Gage, CSE 1622–4GS), a tunable Nd:YAG laser for excitation (duration time of laser pulses 3–5 ns, EKSPILA, NT230–50, equipped with a spectral cleaning unit). The repetition rate of the laser pulses was 2 Hz, intensity of  $\approx 300$   $\mu\text{J cm}^{-2}$ , 20 transients were averaged.

**Fabrication of NaBiS<sub>2</sub> Devices:** The sol-gel solution for ZnO was prepared by dissolving 1 g zinc acetate dihydrate (99.999%, Merck) in 10 mL 2-methoxyethanol (> 99%, Merck) and 284  $\mu\text{L}$  ethanolamine (> 99%, Merck). ITO substrates were cleaned respectively in acetone and isopropanol under ultrasonication for 30 min. The ZnO layer was prepared by spin-coating the sol-gel solution on a cleaned indium tin oxide (ITO) substrate at 3000 rpm for 30 s. Partial ZnO film was wiped off to expose the ITO contact before being annealed at 200 °C for 10 minutes. Later, 40  $\mu\text{L}$  of 20 mg mL<sup>-1</sup> of NaBiS<sub>2</sub> solution was spin-coated onto the ZnO layer at 2000 rpm for 35 s in air. Ligand exchange solutions were prepared by dissolving various iodides (LiI, NaI, KI, and TMAI) in methanol (analytical standard, Merck) to reach a concentration of 0.1 M. During ligand exchange treatment, 40  $\mu\text{L}$  of the ligand exchange solution was dropped onto the spin-coated NaBiS<sub>2</sub> NC film, and then waited for 2 min to ensure the full replacement of the original organic ligands. The film covered by the methanol solution was dried out by spinning at 2000 rpm for 35 s. Next, 40  $\mu\text{L}$  of methanol was dropped onto the film and spined at 2000 rpm for 35 s before 40  $\mu\text{L}$  of toluene was dropped and spined at the same parameters to clean all the residual ligands. After ligand exchange treatment, the NaBiS<sub>2</sub> NC film could no longer be dissolved in toluene, and a thicker NaBiS<sub>2</sub> NC film could be achieved by repetitively performing the procedures described above, namely the “layer-by-layer (LBL)” deposition process. Once the NaBiS<sub>2</sub> film reached a desired thickness, 40  $\mu\text{L}$  of 5 mg mL<sup>-1</sup> PTB7 (1-material) dichlorobenzene (> 99.8%, ROMIL) solution was spin-coated onto it at 2000 rpm for 30 s. Except for the PTB7 layer spin-coated in an N<sub>2</sub>-filled glovebox, all the above deposition processes were performed in air. Finally, 3 nm MoO<sub>x</sub> and 100 nm Ag were evaporated onto the PTB7 layer through a shadow mask, which defined the device area as 4.5 mm<sup>2</sup>. The fabricated devices were exposed in air for at least one night before any further characterization.

**Device Characterization:**  $J-V$  characterisations were conducted by a Keithley 2623A source measure unit (SMU) at a scan rate of 50 mV s<sup>-1</sup>. For the measurements under 1-sun illumination, a 450 W Oriel xenon lamp equipped with a Schott-K113 Tempax sunlight filter (Präzisions Glas & Optik GmbH) was used as the light source. The device area (overlap between

the Ag top electrode and ITO bottom electrode) was 4.5 mm<sup>2</sup>, and the aperture area 3 mm<sup>2</sup>.

For the EQE spectrum acquisition, the measurements were performed on a Bentham PVE300 system, which was calibrated by a silicon photodiode on the transformer mode. During measurements, monochromatic beams with different wavelengths split from a xenon lamp were illuminated on the devices with the two probes contacting the two electrodes.

**X-Ray-Based Measurements:** XRD measurement was performed on a Bruker D8 Advance diffractometer. A Cu K $\alpha$  X-ray source ( $\lambda = 1.5406 \text{ \AA}$ ) was used. Near ambient pressure XPS measurements were conducted in an enviroESCA made by SPECS, which is equipped with a near ambient pressure Phoibos 150 analyzer and 1D delay line detectors. A monochromated Al K $\alpha$  X-ray source ( $\lambda = 8.3386 \text{ \AA}$ ) was utilized. All XPS measurements were conducted in an atmosphere of 7 mbar of N<sub>2</sub> gas. A fast (< 10 s) pump down to vacuum (< 10<sup>-5</sup> mbar) to remove residual air was performed before the venting to 7 mbar with N<sub>2</sub> gas. The pass energies for the XPS survey and high-resolution measurement were 100 and 50 eV, respectively.

**Temperature-Dependent Transient Current Measurements:** Square voltage pulses were generated by a function generator (Hewlett Packard 8116A) and applied to the electron-only device connected in series with a resistor (330  $\Omega$ ). The transient voltage across the resistor was probed by an oscilloscope (RS PRO RSDS1304CFL) and transformed into the transient current. The device was mounted in a Desert TTP4 Probe Station system, which could control the temperature range from 150 K to 360 K via an integrated cryostat. At each temperature, the device was measured after being placed in the Probe Station system for at least 15 min in order to reach thermal equilibrium. In the experiments, the square wave pulses with a voltage amplitude of 2.5 V and a voltage width of 20 ms were utilized.

**Transmission Electron Microscopy:** Transmission electron microscopy (TEM) measurements were performed on JEOL 2100 operated at 200 kV. The samples for TEM characterization were prepared by dropping the NC solution onto carbon-supported copper grids.

## Supporting Information

Supporting Information is available from the Wiley Online Library or from the author.

## Acknowledgements

The authors thank Carola Klimm (HZB) for the cross-sectional SEM measurements, Dennis Friedrich (HZB) and the institute of Solar fuels for providing access to the TRMC and OPTP setups, as well as Peter Nellist (Oxford) for useful discussions. Y.-T.H. would like to thank the Ministry of Education, Taiwan and Downing College Cambridge for funding. Y.-T.H. and R.L.Z.H. acknowledge support from the Silverman Research Fellowship, Downing College Cambridge. M.S. acknowledges the financial support for this work from the Helmholtz International Research School "Hybrid Integrated Systems for Conversion of Solar Energy" (HI-SCORE), an initiative co-funded by the Initiative and Networking Fund of the Helmholtz Association (HIRS-0008). A.M. acknowledges funding received from the European Union's Framework Programme for Research and Innovation HORIZON EUROPE (2021-2027) under the Marie Skłodowska-Curie Action Postdoctoral Fellowships (European Fellowship) 101061809 HyPerGreen. Y.Z. and H.S. acknowledge financial support from the EPSRC Centre for Doctoral Training in Graphene Technology, the Royal Society (RP/R1/201082) and the Engineering and Physical Sciences Research Council (EP/W017091/1). S.J.Z. acknowledges support from the Polish National Agency for Academic Exchange within the Bekker programme (grant no. PPN/BEK/2020/1/00264/U/00001). N.N. acknowledges the Agency for Science, Technology and Research, Singapore for funding. The authors acknowledge support from the Henry Royce Institute (EPSRC grants: EP/P022464/1, EP/R00661X/1), which funded the VXSf Facilities (<https://engineering.leeds.ac.uk/vxsf>) within the Bragg Centre for Materials Research at Leeds University. W.S. acknowledges the David Cockayne

Centre for Electron Microscopy at the University of Oxford. I.L. thanks the AiF project (ZIM-KK5085302DF0) for financial support, and Thomas Dittrich (HZB) for fruitful conversations. R.L.Z.H. would like to thank EPSRC for financial support (grant no. EP/V014498/2), as well as the Royal Academy of Engineering through the Research Fellowships scheme (no. RF\201718\17101).

## Conflict of Interest

The authors declare no conflict of interest.

## Author Contributions

Y.-T.H. and R.L.Z.H. conceived of this work. Y.-T.H. developed and optimized the synthesis of NaBiS<sub>2</sub> NCs, fabricated NaBiS<sub>2</sub> devices, and performed XRD, AFM, TA, temperature-dependent transient current measurements, as well as OPTP and TRMC analyses under the supervision of A.R., R.L.Z.H. and I.L. M.S. and O.S. performed TRMC and ST-TRMC measurements and helped to analyze and interpret the results. H.H. helped with OPTP measurements and helped to analyze the results. Y.Z. helped with the temperature-dependent transient current measurements under the supervision of H.S. M.R. performed steady-state SPV, KP and PYS measurements. A.M. helped with the mobility characterization and analyze the results. I.L. and N.J. performed modulated SPV and transient SPV measurements. I.L. helped to analyze SPV results. S.J.Z. performed PDS measurements under the supervision of S.D.S. A.J.B. performed NAP-XPS measurements. N.N. assisted the NaBiS<sub>2</sub> NC synthesis and film fabrication. W.S. performed the TEM characterization. L.C.H. assisted with the EQE measurements. All authors discussed the results and wrote the paper together.

## Data Availability Statement

The data that support the findings of this study are available under the terms of the CC-BY-4.0 license from <https://dx.doi.org/10.5287/ora-qo5mmj0vg>.

## Keywords

cation disorder, charge-carrier dynamics, ion migration, ligand exchange, nanocrystals, perovskite-inspired materials, ternary chalcogenides

Received: August 28, 2023

Revised: February 4, 2024

Published online: March 19, 2024

- [1] National Renewable Energy Laboratory, Best Research-Cell Efficiency Chart **2022**.
- [2] R. E. Brandt, J. R. Poindexter, P. Gorai, R. C. Kurchin, R. L. Z. Hoye, L. Nienhaus, M. W. B. Wilson, J. A. Polizzotti, R. Sereika, R. Žaltauskas, L. C. Lee, J. L. Macmanus-Driscoll, M. Bawendi, V. Stevanović, T. Buonassisi, *Chem. Mater.* **2017**, 29, 4667.
- [3] R. E. Brandt, V. Stevanović, D. S. Ginley, T. Buonassisi, *MRS Commun.* **2015**, 5, 265.
- [4] Y.-T. Huang, S. R. Kavanagh, D. O. Scanlon, A. Walsh, R. L. Z. Hoye, *Nanotechnology* **2021**, 32, 132004.
- [5] Y. Wang, S. R. Kavanagh, I. Burgués-Ceballos, A. Walsh, D. Scanlon, G. Konstantatos, *Nat. Photonics* **2022**, 16, 235.
- [6] B. A. Rosales, M. A. White, J. Vela, *J. Am. Chem. Soc.* **2018**, 140, 3736.

- [7] Y.-T. Huang, S. R. Kavanagh, M. Righetto, M. Rusu, I. Levine, T. Unold, S. J. Zelewski, A. J. Sneyd, K. Zhang, L. Dai, A. J. Britton, J. Ye, J. Julin, M. Napari, Z. Zhang, J. Xiao, M. Laitinen, L. Torrente-Murciano, S. D. Stranks, A. Rao, L. M. Herz, D. O. Scanlon, A. Walsh, R. L. Z. Hoyer, *Nat. Commun.* **2022**, *13*, 4960.
- [8] P. R. Brown, D. Kim, R. R. Lunt, N. Zhao, M. G. Bawendi, J. C. Grossman, V. Bulovic, *ACS Nano* **2014**, *8*, 5863.
- [9] M. Soreni-Harari, N. Yaacobi-Gross, D. Steiner, A. Aharoni, U. Banin, O. Millo, N. Tessler, *Nano Lett.* **2008**, *8*, 678.
- [10] B. A. Timp, X.-Y. Zhu, *Surf. Sci.* **2010**, *604*, 1335.
- [11] D. Kim, D.-H. Kim, J.-H. Lee, J. C. Grossman, *Phys. Rev. Lett.* **2013**, *110*, 196802.
- [12] O. Voznyy, D. Zhitomirsky, P. Stadler, Z. Ning, S. Hoogland, E. H. Sargent, *ACS Nano* **2012**, *6*, 8448.
- [13] S. J. Oh, N. E. Berry, J.-H. Choi, E. A. Gaubling, T. Paik, S.-H. Hong, C. B. Murray, C. R. Kagan, *ACS Nano* **2013**, *7*, 2413.
- [14] A. M. Medina-Gonzalez, B. A. Rosales, U. H. Hamdeh, M. G. Panthani, J. Vela, *Chem. Mater.* **2020**, *32*, 6085.
- [15] M. M. Bernechea, N. C. Miller, G. Xercavins, D. So, A. Stavrinadis, G. Konstantatos, *Nat. Photonics* **2016**, *10*, 521.
- [16] C. Kim, I. Kozakci, J. Kim, S. Y. Lee, J. Y. Lee, *Adv. Energy Mater.* **2022**, *2200262*, 2.
- [17] H. Shinotsuka, S. Tanuma, C. J. Powell, D. R. Penn, *Surf. Interface Anal.* **2015**, *47*, 871.
- [18] M. Rusu, T. Kodalle, L. Choubrac, N. Barreau, C. A. Kaufmann, R. Schlattmann, T. Unold, *ACS Appl. Mater. Interfaces* **2021**, *13*, 7745.
- [19] I. Levine, O. G. Vera, M. Kulbak, D.-R. Ceratti, C. Rehmann, J. A. Marquez, S. Levchenko, T. Unold, G., *ACS Energy Lett.* **2019**, *4*, 1150.
- [20] E. Zillner, S. Fengler, P. Niyamakom, F. Rauscher, K. Kohler, T. Dittrich, *J. Phys. Chem. C* **2012**, *116*, 16747.
- [21] A. D. Wright, L. R. VBuizza, K. J. Savill, G. Longo, H. J. Snaith, M. B. Johnston, L. M. Herz, *J. Phys. Chem. Lett.* **2021**, *12*, 3352.
- [22] M. Schleuning, M. Kölbach, I. Ahmet, R. Präg, R. Gottesman, R. Gunder, M. Zhang, D. R. Wargulski, D. Abou-Ras, D. A. Grave, F. F. Abdi, R. van deKrol, K. Schwarzburg, R. Eichberger, D. Friedrich, H. Hempel, *Adv. Funct. Mater.* **2023**, *33*, 2300065.
- [23] S. Gräbtchak, M. Cocivera, *Philos. Mag. B* **1999**, *79*, 49.
- [24] S. Gräbtchak, M. Cocivera, *Phys. Rev. B* **1998**, *58*, 12594.
- [25] A. D. Wright, R. L. Milot, G. E. Eperon, H. J. Snaith, M. B. Johnston, L. M. Herz, *Adv. Funct. Mater.* **2017**, *27*, 1700860.
- [26] S. Gahlawat, I. Y. Ahmet, P. Schnell, I. Levine, S. Zhang, P. P. Ingole, F. F. Abdi, *Chem. Mater.* **2022**, *34*, 4320.
- [27] M. Kölbach, I. J. Pereira, K. Harbauer, P. Plate, K. Höflich, S. P. Berglund, D. Friedrich, R. van deKrol, F. F. Abdi, *Chem. Mater.* **2018**, *30*, 8322.
- [28] M. Schleuning, M. Kölbach, F. F. Abdi, K. Schwarzburg, M. Stollerfoht, R. Eichberger, R. van deKrol, D. Friedrich, H. Hempel, *PRX Energy* **2022**, *1*, 23008.
- [29] K. A. Bush, N. Rolston, A. Gold-Parker, S. Manzoor, J. Hausele, Z. J. Yu, J. A. Raiford, R. Cheacharoen, Z. C. Holman, M. F. Toney, R. H. Dauskardt, M. D. McGehee, *ACS Energy Lett.* **2018**, *3*, 1225.
- [30] Y. Peng, T. N. Huq, J. Mei, L. Portilla, R. A. Jagt, L. G. Occhipinti, J. L. MacManus-Driscoll, R. L. Z. Hoyer, V. Pecunia, *Adv. Energy Mater.* **2021**, *11*, 2002761.
- [31] Irfan, H. D., Y. Gao, C. Small, D. Y. Kim, J. Subbiah, F. So, *Appl. Phys. Lett.* **2010**, *96*, 116.
- [32] C. Eames, J. M. Frost, P. R. F. Barnes, B. C. O'Regan, A. Walsh, M. S. Islam, *Nat. Commun.* **2015**, *6*, 2.
- [33] H. Zai, Y. Ma, Q. Chen, H. Zhou, *J. Energy Chem.* **2021**, *63*, 528.
- [34] B. Chen, M. Yang, S. Priya, K. Zhu, *J. Phys. Chem. Lett.* **2016**, *7*, 905.
- [35] H. Wang, Z. Xie, X. Wang, Y. Jia, *Catalysts* **2020**, *10*, 413.
- [36] V. M. LeCorre, J. Diekmann, F. Peña-Camargo, J. Thiesbrummel, N. Tokmoldin, E. Gutierrez-Partida, K. P. Peters, L. Perdigón-Toro, M. H. Futscher, F. Lang, J. Warby, H. J. Snaith, D. Neher, M. Stollerfoht, *Sol. RRL* **2022**, *6*, 2100772.
- [37] W. Pan, H. Wu, J. Luo, Z. Deng, C. Ge, C. Chen, X. Jiang, W. Yin, G. Niu, L. Zhu, L. Yin, Y. Zhou, Q. Xie, X. Ke, *Nat. Photonics* **2017**, *11*, 726.
- [38] Z. Li, S. P. Senanayak, L. Dai, G. Kusch, R. Shivanna, Y. Zhang, D. Pradhan, J. Ye, Y. T. Huang, H. Sirringhaus, R. A. Oliver, N. C. Greenham, R. H. Friend, R. L. Z. Hoyer, *Adv. Funct. Mater.* **2021**, *31*, 2104981.
- [39] Y. T. Huang, D. Nodari, F. Furlan, Y. Zhang, M. Rusu, L. Dai, Z. Andaji-Garmaroudi, D. Darvill, X. Guo, M. Rimmele, T. Unold, M. Heeney, S. D. Stranks, H. Sirringhaus, A. Rao, N. Gasparini, R. L. Z. Hoyer, *Small* **2023**, *2310199*.
- [40] D. Li, H. Wu, H.-C. Cheng, G. Wang, Y. Huang, X. Duan, *ACS Nano* **2016**, *10*, 6933.
- [41] M. Berruet, J. C. Pérez-Martínez, B. Romero, C. Gonzales, A. M. Al-Mayouf, A. Guerrero, J. Bisquert, *ACS Energy Lett.* **2022**, *7*, 1214.
- [42] C. Gonzales, A. Guerrero, J. Bisquert, *J. Phys. Chem. C* **2022**, *126*, 13560.
- [43] Y. Lu, Y. Mi, J. Li, F. Qi, S. Yan, W. Dong, *Nanomaterials* **2021**, *11*, 2290.
- [44] X. He, Q. Bai, Y. Liu, A. M. Nolan, C. Ling, Y. Mo, *Adv. Energy Mater.* **2019**, *9*, 1902078.
- [45] C. A. Sebenne, *Nuovo Cim. B Ser.* **1977**, *39*, 768.
- [46] T. Dittrich, S. Fengler, *Surface photovoltage analysis of photoactive materials*, World scientific, Singapore **2019**.